Electrodynamic response in the electronic nematic phase of $BaFe_2As_2$

C. Mirri,[1,*] A. Dusza,[1] S. Bastelberger,[1] M. Chinotti,[1] J.-H. Chu,[2,3] H.-H. Kuo,[2,3] I. R. Fisher,[2,3] and L. Degiorgi[1,*]

[1]*Laboratorium für Festkörperphysik, ETH - Zürich, 8093 Zürich, Switzerland*

[2]*Geballe Laboratory for Advanced Materials and Department of Applied Physics, Stanford University, Stanford, California 94305, USA*

[3]*Stanford Institute for Materials and Energy Sciences, SLAC National Accelerator Laboratory, 2575 Sand Hill Road, Menlo Park, California 94025, USA*

(Received 23 October 2015; published 5 February 2016)

We perform, as a function of uniaxial stress, a temperature-dependent optical-reflectivity investigation of the parent Fe-arsenide compound $BaFe_2As_2$ over a broad spectral range, from the far infrared up to the ultraviolet, across the coincident structural tetragonal-to-orthorhombic and spin-density-wave (SDW) phase transitions at $T_{s,N} = 135$ K. Our results provide knowledge to the complete electrodynamic response of the title compound over a wide energy range as a function of both tunable variables. For temperatures below $T_{s,N}$, varying the uniaxial stress *in situ* affects the twin domain population and yields hysteretic behavior of the optical properties as the stress is first increased and then decreased, whereas for temperatures above $T_{s,N}$ the stress-induced optical anisotropy is reversible, as anticipated. In particular, by analyzing the low-frequency infrared response, we obtain detailed insight to the effects determining the intrinsic anisotropy of the (metallic) charge dynamics in the orthorhombic state, and similarly the induced one due to applied uniaxial stress at higher temperatures in the tetragonal phase. The low-frequency optical conductivity thus allows establishing a link to the *dc* transport properties and reveals that they are determined almost exclusively by changes in the Drude weight, therefore by the anisotropy in the Fermi surface parameters. Finally, we show that the spectral weight distribution in the SDW state occurs for energies below approximately 1 eV, and therefore points towards a correlation mechanism due to Hund's coupling rather than on-site Coulomb interactions.

DOI: 10.1103/PhysRevB.93.085114

I. INTRODUCTION

A peculiarity of many Fe-arsenide and chalcogenide superconductor families in their underdoped regime is the ferroelasticlike structural transition at T_s, from a tetragonal to an orthorhombic phase, which breaks the four-fold rotational symmetry of the high-temperature crystal lattice, implying the onset of a nematic phase [1,2]. In several compounds, the structural transition is accompanied by a spin-density-wave (SDW) phase transition at $T_N \leqslant T_s$, which in $BaFe_2As_2$ leads to ordered stripes with the spins aligned antiferromagnetically (AFM) along the elongated *a* axis and ferromagnetically (FM) along the shorter *b* axis. The origin of the nematic phase is still a matter of debate and different theories, based on orbital ordering, spin-driven mechanisms and a Pomeranchuk-type instability, have been proposed [3–14].

In order to minimize the elastic energy, dense structural twins form at temperatures below T_s, which mask the anticipated in-plane anisotropy of measurable physical quantities in the orthorhombic phase. Such an anisotropy can be recovered by aligning the domains along a preferential direction (i.e., by detwinning the specimens), which may be achieved in large magnetic fields or by exerting uniaxial stress [1,2,15,16]. Over the past few years, many efforts [17–49] have been made in exploring the nematic phase in single domain specimens with local probes or in fully detwinned crystals, which were constantly held under a fixed applied pressure by using a mechanical clamp. It was soon realized that being able to modulate the strength of the applied anisotropic strain was crucial in order to (a) determine the effect of strain in the high-symmetry tetragonal phase (and hence determine the nematic susceptibility) and (b) dynamically vary the twin population in the broken-symmetry state below T_s (and hence establish hysteretic effects associated with twin boundary motion). Elastoresistance measurements, probing the response to anisotropic strain in the tetragonal state [50–52], have been effected using a piezoelectric stack to dynamically tune the strain. This technique is especially well suited to the temperature regime above T_s, but is not ideal for probing the response below T_s [53]. We recently developed a complementary technique using a gas-bellows to tune the uniaxial stress that is exerted on samples, which is far better than the piezoelectric stack for the regime below T_s [54,55].

Our optical reflectivity measurement, as a function of temperature and *in situ* tunable uniaxial pressure, is in principle an excellent probe in order to study the impact of the nematic phase on the charge dynamics and electronic properties, since it spans a vast energy interval, extending from the Fermi surface (FS) to energies deep into the electronic structure. Our previous work, limited to the mid-infrared (MIR) spectral range in the underdoped regime of $Ba(Fe_{1-x}Co_x)_2As_2$, pointed out the remarkable fingerprint of the nematic state at energy scales far away from the Fermi level, even suggesting that superconductivity in the underdoped regime emerges from an electronic polarized state [54,55]. We furthermore discovered a hysteretic optical anisotropy as a function of applied pressure in the orthorhombic phase due to the motion of the nematic domain walls, crossing over to a linear and reversible stress dependence in the tetragonal state [54,55]. We proposed the analogy with a ferromagnet in order to account for the optical anisotropy upon modulating uniaxial compressive stress, so that by releasing pressure *in situ*, we were able

*Correspondence and requests for materials should be addressed to: chiara@phys.ethz.ch, degiorgi@solid.phys.ethz.ch

to observe the remanent anisotropy of the electrodynamic response at temperatures well below T_s for unstressed but fully detwinned crystals. We also provided an optical estimation of the "ferroelastic" susceptibility, which shows a divergence at T_s [54], in broad accord with the nematic susceptibility inferred from the dc results [50,56]. Such an optical fingerprint of the nematic fluctuations further supports the electronic nature of the structural transition.

Here, we investigate the in-plane optical reflectivity of the parent compound $BaFe_2As_2$ beyond the MIR interval studied so far, covering the spectral range from the far infrared (FIR) to the ultraviolet (UV), at several combinations of uniaxial pressure (p) and temperature (T). This is the prerequisite, which allows extracting the optical conductivity via Kramers-Kronig transformations of the reflectivity data. Our goal is to probe the anisotropic response in its real part $\sigma_1(\omega)$. It has been already shown that a remarkable anisotropy of $\sigma_1(\omega)$ develops in the orthorhombic phase for specimen constantly held under uniaxial compressive stress [44–47]. Therefore it is of interest to elucidate how such an anisotropy specifically evolves in the metallic optical response as a function of the external uniaxial pressure and across the structural transition. In that context, we particularly analyze the effective metallic component of $\sigma_1(\omega)$ and we study the consequences of the spectral-weight reshuffling over a large energy interval. This paper also serves the purpose to complement the experimental findings and the discussion in our preceding letter [57], devoted to shed light on the origin of the dc resistive anisotropy. We thus provide a comprehensive elaboration of the electrodynamic response with respect to the electronic nematic phase, induced upon tuning *in situ* and in a controlled way the symmetry breaking uniaxial compressive stress.

II. SAMPLE AND EXPERIMENT

The $BaFe_2As_2$ single crystal was grown using a self-flux method [58]. It has a square-plate shape with a thickness of 0.2 mm and a side of approximately 2 mm, with the c axis perpendicular to the plane of the plate and the tetragonal a axis oriented at 45° with respect to the edges of the sample, so that below T_s the orthorhombic a/b axes are parallel to the sides of the square [1,17]. The structural and magnetic transition occur at $T_s = T_N = 135$ K (from now on denoted as $T_{s,N}$) [1].

The reflectivity $R(\omega)$ was measured at nearly normal incidence with the electromagnetic radiation polarized along the a and b axes. First we collected data at 300 K with a Bruker IFS48 interferometer for the MIR (i.e., $\omega \sim$ 500–5000 cm^{-1}) and a PerkinElmer Lambda 950 spectrometer up to the UV (i.e., $\omega \sim$ 3200–40000 cm^{-1}) range. The specimen was then mounted into the pressure device and placed inside an Oxford SM 4000 cryostat coupled to a Bruker Vertex 80v, Fourier-transform infrared interferometer. The device, described in Refs. [54,55], consists of a spring bellows connected through a capillary to a pipeline outside the cryostat. The bellows can be extended/retracted by flushing He gas into its volume or evacuating it through the pipeline, thus exerting and releasing uniaxial pressure on the lateral side of the specimen (see Fig. 1 of Ref. [55]). The uniaxial pressure, detwinning the samples, is thus applied parallel to the orthorhombic b axis, which is preferentially aligned along the direction of a compressive stress. Here, we refer to the He-gas pressure inside the volume of the bellows: the effective pressure felt by the sample depends on its size and thickness, so that a He-gas pressure of 0.1 bar on our $BaFe_2As_2$ crystal means an effective pressure of about 1.5 MPa.

Data were collected from $\omega \sim 60$ to 7000 cm^{-1} as a function of both T and p, through different experimental protocols [54]. Here, we report results obtained from the so-called zero-pressure-cooled (ZPC) experiment, reminiscent of the zero-field-cooling procedure for magnetization measurements in a ferromagnet. From above $T_{s,N}$ we cool down the sample to the selected temperature, without applying any uniaxial compressive stress. At that T, kept fixed during the whole experiment, we progressively increase p in steps of 0.2 bar from 0 to a maximum of 0.8 bar and measure $R(\omega)$ at each step. Then, we complete the "pressure loop" by measuring $R(\omega)$ when releasing p back to 0 bar. The sample was thermalized at $T \gg T_{s,N}$ before performing a ZPC for the next measurement at a different temperature. Further details about the experimental technique and setup can be found in Ref. [54] and its Supplemental Material as well as in Ref. [55]. The optical conductivity was then extracted from the reflectivity spectrum by Kramers-Kronig (KK) transformations [59]. We made use of the standard $R(\omega) \sim \omega^{-s}$ (with $2 < s < 4$) extrapolation at high frequencies (i.e., $\omega >$ 40000 cm^{-1}), while the $R(\omega \to 0)$ values were obtained by merging the measured data with the Hagen-Rubens (HR) extrapolation $[R(\omega) = 1 - 2\sqrt{\frac{\omega}{\sigma_{dc}}}]$ in the energy interval between 80 and 100 cm^{-1}, depending from the data quality at different combinations of T and p [59]. The σ_{dc} values, used for the HR extrapolation of $R(\omega)$, are in good agreement with the dc transport measurements [17,50].

III. EXPERIMENTAL RESULTS

The in-plane reflectivity $R(\omega)$ of $BaFe_2As_2$ is shown in Fig. 1 at selected T and p. In the upper right panel (a), the temperature evolution at 0 bar (i.e., unstressed, twinned case) of $R(\omega)$ is displayed in a semilogarithmic scale, in the whole spectral range under investigation. For $\omega \leqslant 80$ cm^{-1}, we can appreciate the smooth crossover to the HR extrapolation at all T. The $R(\omega)$ spectra at $T > T_{s,N}$ reveal a typical overall metallic behavior, for which $R(\omega)$ merges towards total reflection for frequencies tending to zero, accompanied by a broad absorption feature at high frequencies (i.e., around 6000–7000 cm^{-1}). Below $T_{s,N}$, the SDW order partially suppresses $R(\omega)$ between 200 and 1000 cm^{-1}, as a consequence of the partial-gap opening in the magnetic state [44,45,60], while below 200 cm^{-1} an upturn in $R(\omega)$ occurs so that $R(\omega \to 0) \to 100\%$, recovering a metallic behavior. Consequently, above 1000 cm^{-1} there is a temperature dependent absorption feature, exhausting above 2500 cm^{-1}, where all spectra merge together as for $T > T_{s,N}$.

The p evolution of $R(\omega)$ at selected T is highlighted in panels (b) to (u) of Fig. 1 for frequencies up to 2500 cm^{-1}. Each panel compares $R(\omega)$ for a selected combination of p and T with the spectra at 160 K, at the same p, for both polarization directions (i.e., a and b axes). We choose 160 K as reference temperature, since the $R(\omega)$ spectra are fully

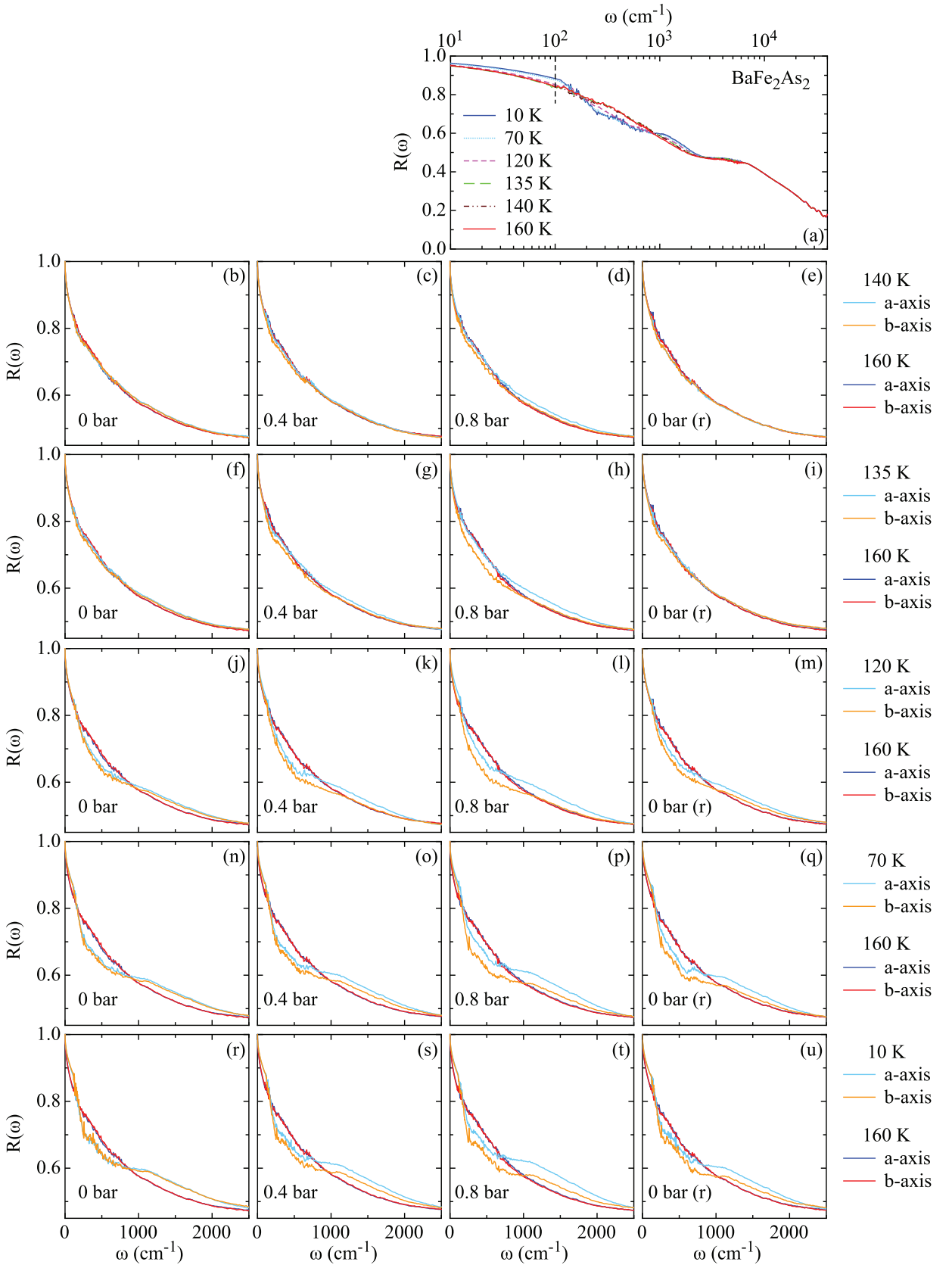

FIG. 1. In-plane reflectivity [$R(\omega)$] of $BaFe_2As_2$ at selected T and p. (a) Temperature evolution of $R(\omega)$ in the FIR-UV range (semilogarithmic scale) for twinned samples (i.e., at 0 bar). The vertical dashed line marks the upper frequency limit of the HR extrapolation (see text). (b)–(u) display the pressure dependence of the optical anisotropy in $R(\omega)$ up to 2500 cm^{-1} collected at 0, 0.4, 0.8 and released 0 bar [denoted by "(r)"] and at selected T: (b)–(e) 140, (f)–(i) 135, (j)–(m) 120, (n)–(q) 70, and (r)–(u) 10 K, compared to the data collected at 160 K for equivalent p.

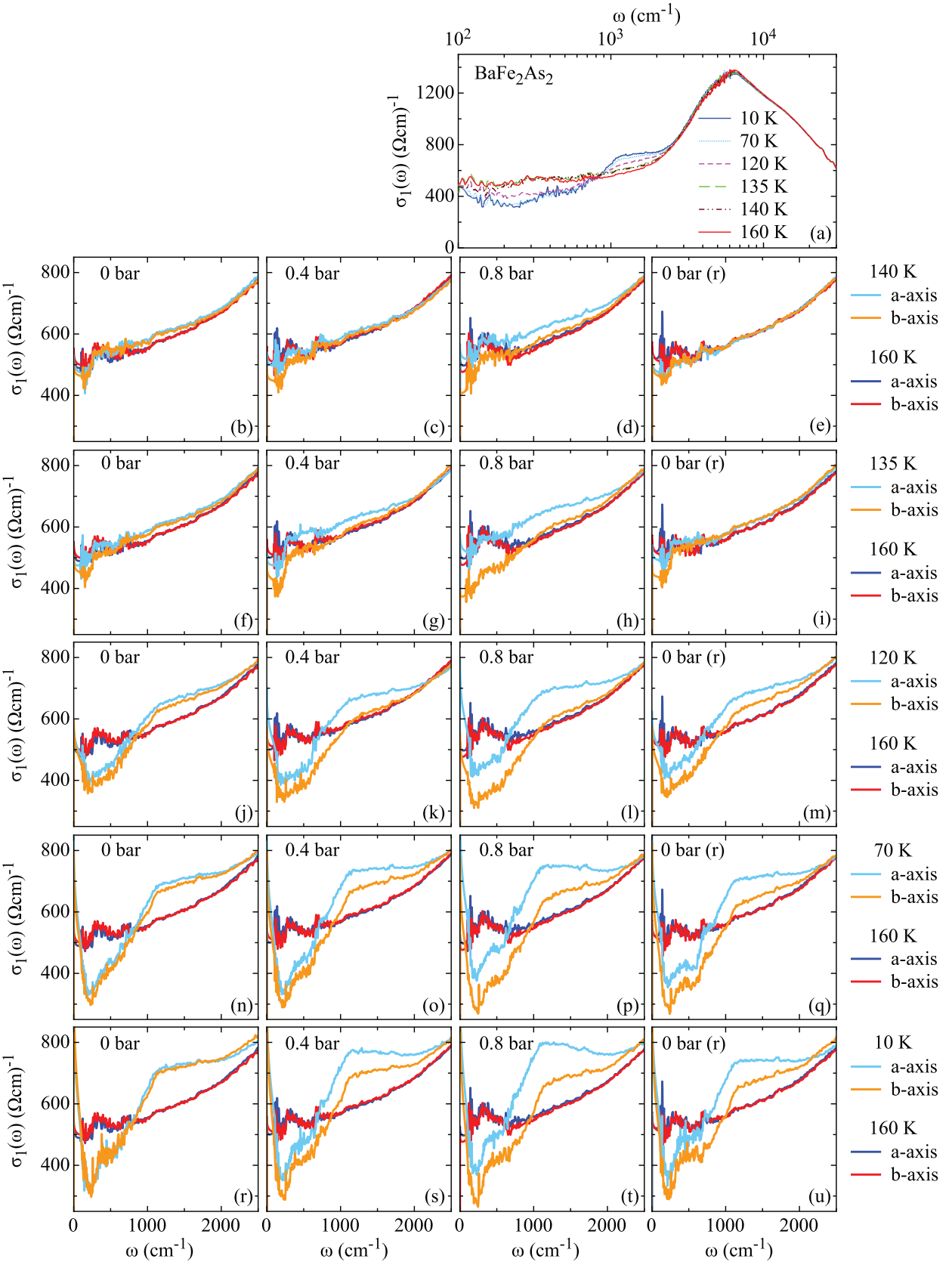

FIG. 2. In-plane optical conductivity of $BaFe_2As_2$ at selected T and p. (a) Temperature evolution of $\sigma_1(\omega)$ in the FIR-UV range (semilogarithmic scale) at 0 bar (i.e., twinned sample) [57]. (b)–(u) display the pressure evolution of the anisotropy in $\sigma_1(\omega)$ up to 2500 cm^{-1} at 0, 0.4, 0.8 [57] and released 0 bar [denoted by "(r)"] and at selected T: (b)–(e) 140, (f)–(i) 135, (j)–(m) 120, (n)–(q) 70, and (r)–(u) 10 K, compared to the data at 160 K for equivalent p. We apply the same legend convention as in Fig. 1.

isotropic at $T > 160$ K for any p. Therefore each panel of a given row displays data at (from left to right) $p = 0$ bar, 0.4 bar, 0.8 bar and released 0 bar at a fixed T [e.g., (b)–(e) at 140 K] and at 160 K for both axes. This allows conveying the pressure-dependent reversibility at $T > T_s$ as well as the pressure-dependent irreversibility below T_s of the optical anisotropy. In the unstressed case ($p = 0$ bar), no anisotropy is detected at all T, as an effect of the twin domains in the specimen. As anticipated above, one can clearly observe the depletion below 1000 cm^{-1} and the overshoot exhausting at 2500 cm^{-1} with decreasing T below $T_{s,N}$, due to the SDW-gap formation [61]. Upon applying p, $R(\omega)$ displays an anisotropy which is enhanced when lowering T. By increasing p up to 0.8 bar, the anisotropy in $R(\omega)$ saturates at $T < T_{s,N}$ being the sample fully detwinned. Upon releasing p, we observe a persisting optical anisotropy in $R(\omega)$ for $T \ll T_{s,N}$, even when reducing the compressive stress back to 0 bar (remanent state). As shown in Refs. [54] and [55], this shapes a so-called hysteretic behavior in the optical anisotropy, which tends to collapse for $T \to T_{s,N}$. It is worth noting that the anisotropic optical response starts to develop already below 160 K (i.e., at $T \geqslant T_{s,N}$) for $p \geqslant 0.4$ bar [Figs. 1(d), 1(g), and 1(h)]. Above $T_{s,N}$, the $R(\omega)$ anisotropy turns out to be weak and fully reversible upon sweeping p and disappears as soon as p is completely released back to 0 bar [54,55].

The optical conductivity, extracted from $R(\omega)$ through KK transformations, is shown in Fig. 2 for equivalent combinations of p and T as in Fig. 1. The upper right panel (in a semilogarithmic scale) displays the temperature evolution of $\sigma_1(\omega)$ in the unstressed (twinned) case and for $\omega \geqslant 100$ cm^{-1}, thus in the whole spectral range under investigation. The overall behavior of $\sigma_1(\omega)$ is in good agreement with previous results [45,60,61], obtained in the case of twinned crystals. At $T \geqslant T_{s,N}$, $\sigma_1(\omega)$ is weakly temperature dependent, tending to a constant value in the FIR range, as it is common for a metal. Below $T_{s,N}$, the transition into the SDW state opens a partial gap, which depletes $\sigma_1(\omega)$ in FIR below 1000 cm^{-1} and, due to the reshuffled spectral weight (see below), leads to its enhancement at MIR frequencies, forming a peak centered at about 1300 cm^{-1}. The ungapped portion of the FS contributes to the metallic response of $\sigma_1(\omega)$ merging into a narrow zero-energy mode below 200 cm^{-1}. Such a strong temperature dependence in the optical conductivity, due to the SDW order, expires above 3000 cm^{-1}. The peak around 7000 cm^{-1} can be ascribed to electronic interband transitions [44,45,62–64].

The panels from (b) to (u) in Fig. 2 highlight the p dependence of $\sigma_1(\omega)$ up to 2500 cm^{-1} along both crystallographic directions. Each panel corresponds to a selected combination of p and T, allowing a comparison with $\sigma_1(\omega)$ at 160 K at the same p. We apply the same layout as for Fig. 1. A complementary display of $\sigma_1(\omega)$ for both axes as well as of the dichroism (i.e., $\sigma_1^a(\omega, p; T) - \sigma_1^b(\omega, p; T)$) as a function of p at selected T is presented in Fig. 7 of the Appendix (see also Fig. 1 of Ref. [57]). At 0 bar, $\sigma_1(\omega)$ shows no significant anisotropy at all temperatures. When pressure is applied, a rising optical anisotropy is clearly observed upon lowering T. Along the a axis, the depletion in FIR becomes less pronounced, the intensity of the MIR absorption increases and its peak frequency shifts to lower energy upon increasing p. Quite the opposite behavior is observed along the b axis. This leads to an overall optical anisotropy, which saturates at 0.8 bar for $T \ll T_{s,N}$ [57]. Upon releasing the compressive stress back to zero, a remanent anisotropy can be still observed at $T < T_{s,N}$, but it fully collapses at $T \cong T_{s,N}$. In other words, we can be certain that the orthorhombic state is strongly anisotropic even in the absence of any external strain. A weakly p-dependent anisotropy in $\sigma_1(\omega)$ is observable already at $T_{s,N} \lesssim T < 160$ K for $p \geqslant 0.4$ bar [Figs. 2(d), 2(g), and 2(h)] and turns out to be reversible upon sweeping p.

IV. ANALYSIS AND DISCUSSION

A. Drude-Lorentz fit

In order to analyze our results, we fit the optical response functions, for all combinations of p and T, by means of the phenomenological Drude-Lorentz model [59]. The fit components for $\sigma_1(\omega)$ are displayed in Fig. 3 [57]. As confirmed by the optical work of several groups [65], it is well recognized that a generic low-frequency optical feature of the ferropnictide materials consists in a metallic zero-energy mode, merging into a broad tail up to about 1000 cm^{-1} in $\sigma_1(\omega)$ [see, e.g., Fig. 2(a)]. In principle that tail can be fitted with a very broad, low-frequency harmonic oscillator (HO). This latter HO would have such a low resonance frequency (i.e., ω_0 less than 50 cm^{-1}) so that it actually resembles a Drude response. While low-energy interband transitions are expected for the ferropnictide [66–68], they are not expected to fall below 50 cm^{-1} and as such they would be rather unphysical. A single

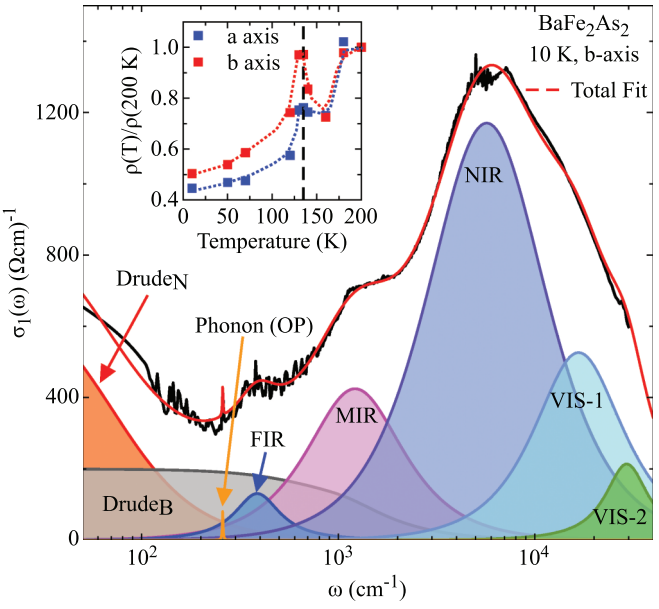

FIG. 3. Fit components of the optical conductivity along the b axis in $BaFe_2As_2$, at 10 K and 0 bar (see also Fig. 2(g) in Ref. [57]), considered within the Drude-Lorentz approach [Eq. (1)]. Apart from the optical phonon (OP) contribution, an equivalent set of fit components is considered along the a axis. (Inset) Temperature dependence of $\rho(T) = [\sigma_1(\omega = 0, T)]^{-1}$ from the fit (see text) of the optical conductivity at 0.8 bar (i.e., at saturation). Each resistivity curve has been normalized at 200 K. The dashed line indicates the transition temperature $T_{s,N}$, while the dotted lines are guide to the eyes.

Drude component as well as the generalized Drude approach are therefore not appropriate because of the multiband nature of the ferropnictide coupled with the Drude-like shape of the (artificial) low-frequency HO. This led indeed to the fit procedure, which models the free-carriers response as two separate, uncorrelated electronic subsystems, described by a broad and a narrow Drude term (Drude_B and Drude_N, respectively), rather than a single dominant band.

At finite frequency we add three HOs FIR, MIR, and NIR for the respective spectral ranges and two high-frequency and temperature-independent HOs covering the energy interval from the visible up to the UV range (VIS-1, VIS-2). The HOs generally account for the electronic interband transitions, predicted on various occasions and widely discussed in the literature [62,63]. Particularly, the FIR and MIR HOs describe low-energy interband transitions interplaying with the Drude components, as anticipated above, and finally merging into the SDW gap excitation at low temperatures [66–68]. We are convinced that our phenomenological fit procedure allows us appropriately disentangling the electronic interband contributions from the metallic Drude terms. We use the same set of components at all T and p as well as for both polarization directions, with the exception of the optical phonon (OP) which appears only along the b axis at $T < T_{s,N}$. At low temperatures, $\sigma_1(\omega)$ is depleted due to the SDW transition, thus allowing the detection of the lattice vibration peaked at about 260 cm^{-1} at $T \ll T_{s,N}$ [47,69], while at $T > T_{s,N}$ there is a total screening of the phonon mode by the itinerant charge-carriers contribution, as it occurs along the a axis at all temperatures. Schafgans *et al.* studied in great depth the optical IR-active phonons coupled to the free electron response in the orthorhombic phase of the title compounds [69]. Besides screening, they additionally proposed that the overall phonon spectral weight behavior may be the direct consequence of Hund's rule coupling. We will return later to the Hund's rule coupling issue, when discussing our findings within their spectral weight analysis.

By recalling that the complex optical conductivity relates to the complex dielectric function as $\tilde{\epsilon} = \epsilon_1 + i\epsilon_2 = \epsilon_\infty + 4\pi i(\sigma_1 - i\sigma_2)/\omega$, we can summarize our fit procedure as follows:

$$\begin{aligned}\tilde{\epsilon} = \epsilon_\infty &- \frac{\omega_{pN}^2}{\omega^2 + i\omega\Gamma_N} - \frac{\omega_{pB}^2}{\omega^2 + i\omega\Gamma_B} \\ &+ \frac{S_{\text{FIR}}^2}{\omega_{0,\text{FIR}}^2 - \omega^2 - i\omega\gamma_{\text{FIR}}} + \frac{S_{\text{MIR}}^2}{\omega_{0,\text{MIR}}^2 - \omega^2 - i\omega\gamma_{\text{MIR}}} \\ &+ \frac{S_{\text{NIR}}^2}{\omega_{0,\text{NIR}}^2 - \omega^2 - i\omega\gamma_{\text{NIR}}} + \sum_{j=1}^{2} \frac{S_j^2}{\omega_{0,j}^2 - \omega^2 - i\omega\gamma_j} \\ &+ \frac{S_{\text{OP}}^2}{\omega_{0,\text{OP}}^2 - \omega^2 - i\omega\gamma_{\text{OP}}}. \end{aligned} \quad (1)$$

In Eq. (1), ϵ_∞ is the optical dielectric constant. The last term in Eq. (1) is only added for the analysis of the optical response along the b axis, as it describes the OP contribution. $\Gamma_{N/B}$ and $\omega_{pN/B}$ of the narrow (N)/broad (B) Drude terms are, respectively, the width at half maximum (scattering rate) and the plasma frequency ($\omega_p = \sqrt{\frac{4\pi e^2 n}{m^*}}$) of the itinerant charge carriers, with charge e, density n and effective mass m^*. The parameters for each HO at finite frequency are the strength (S), the center-peak frequency (ω_0) and the width (γ). Within this phenomenological approach we simultaneously fit both $R(\omega)$ and $\sigma_1(\omega)$, achieving a good reproduction of the optical functions, as shown for example in Fig. 3 for $\sigma_1(\omega)$ at 10 K and 0 bar along the b axis. The overall fitting procedure is consistent with our previous analysis [44,45] and is pretty well established in the literature [65].

The parameters $\omega_{pN/B}$ and $\Gamma_{N/B}$, describing the two Drude components, are shown in Fig. 4 for both crystallographic directions as a function of p and T [57]. Table I and Fig. 8 to 10 in the Appendix summarize the HOs parameters. A first-neighbor interpolation of the experimental points (full dots) was used in order to generate the color maps. The narrow Drude component, which is obviously tied to the necessary HR extrapolation for the purpose of the KK transformations, is rather isotropic between both axes at all T and p. The corresponding Drude plasma frequency ω_{pN} is p- and T-independent, while the scattering rate Γ_N gets suppressed in a similar fashion along both axes upon crossing the structural and SDW phase transition at any degree of detwinning. This indicates a quite pronounced narrowing of $\sigma_1(\omega)$ below 200 cm^{-1} upon lowering T. We may state that this narrow Drude term accounts for the itinerant charge carriers, which are not gapped by the SDW transition and belong to fully isotropic band even in the orthorhombic phase. The reduced scattering below $T_{s,N}$ bears however testimony to a SDW-induced suppression of scattering channels also for that portion of FS.

On the contrary, the broad Drude term turns out to be largely anisotropic below $T_{s,N}$ and thus very much affected by the degree of detwinning. Below $T_{s,N}$ and for $p \leqslant 0.2$ bar, both plasma frequency and scattering rate decrease monotonically with T, as an effect of the FS gapping and the suppression of scattering channels due to the SDW transition, respectively. Since the specimen is not yet fully detwinned for $p \leqslant 0.2$ bar, the overall depletion of both (broad) Drude parameters reflects an average behavior of those quantities for all crystallographic directions. Upon detwinning the specimen (i.e., for $p \geqslant 0.2$ bar) the anisotropy of ω_{pB} and Γ_B develops along the orthorhombic axes. Along the a axis both plasma frequency and scattering rate are enhanced with respect to the b axis parameters, which instead get further suppressed and depleted at $T < T_{s,N}$ and upon increasing p. We also observe that the anisotropy in ω_{pB} and Γ_B parameters achieved at saturation (i.e., at 0.8 bar, where the sample is totally detwinned [54,55,70]) almost fully persists in the remanent phase (i.e., at zero released p) below $T_{s,N}$. The result of our fits at saturation and $T \leqslant T_{s,N}$ is in very good agreement with the previous analysis of the effective metallic response performed on specimens constantly held under uniaxial pressure [44,45].

From the fit parameters of the two Drude terms, one can reconstruct the dc limit of the optical conductivity $\sigma_1(\omega = 0, T) = \frac{\omega_{pB}^2}{4\pi\Gamma_B} + \frac{\omega_{pN}^2}{4\pi\Gamma_N}$ thus allowing a comparison with the dc transport measurements. The temperature dependence of $\rho(T) = [\sigma_1(\omega = 0, T)]^{-1}$, normalized at 200 K, is shown in the inset of Fig. 3 for $p = 0.8$ bar [70] and is in very good agreement with the transport data collected on samples constantly held under uniaxial compressive stress [17]. The

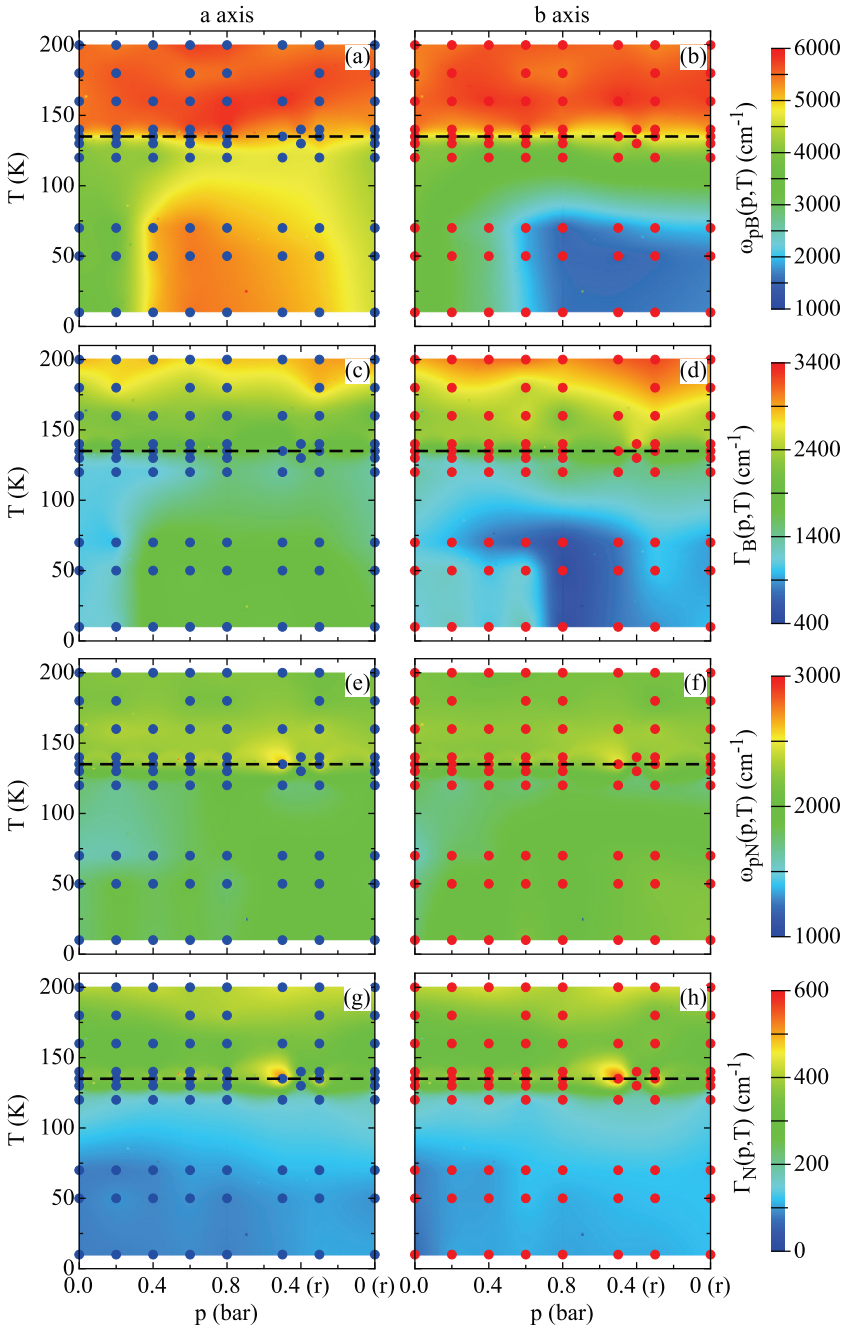

FIG. 4. Pressure and temperature dependence of the parameters describing the Drude components [57]. The panels show: [(a), (b), (e), and (f)] the plasma frequency ($\omega_{pN/B}$) and [(c), (d), (g), and (h)] the scattering rate ($\Gamma_{N/B}$) of the broad (B) and narrow (N) Drude term along the a and b axes, respectively. The dots indicate the fitted (p,T) points, which have been interpolated using a first-neighbor interpolation procedure to generate the color maps. The dashed line indicates the transition temperature $T_{s,N}$. Released pressures are denoted by "(r)."

full T as well as p dependence of the dc resistivity, as evinced from our fit parameters, is discussed in Ref. [57]. Here, we emphasize that the stress-induced dc anisotropy develops already at $T \leqslant 160$ K (thus above $T_{s,N}$) in agreement with Ref. [17]. Our preceding letter [57] elaborates on the ongoing experimental debate [20,38,39,47,51,52], also reflected in an ample theoretical activity (see below), as to whether the dc anisotropy in the nematic phase ($T_N < T < T_s$) or in the tetragonal phase above T_s in the presence of an external symmetry breaking field is primarily determined by the Fermi surface (i.e., Drude weight) or scattering rate anisotropy. We show in Ref. [57] that the dc resistivity anisotropy is dominated by the anisotropy in the Drude spectral weight (i.e., $\omega_{pN}^2 + \omega_{pB}^2$) rather than in the scattering rate. In the SDW state, both the scattering rate and spectral weight contribute to the dc resistivity anisotropy, but the spectral weight is the dominant effect. However, in the tetragonal phase the strain-induced elastoresistance anisotropy is almost completely determined by the spectral weight anisotropy. This result definitively establishes that the primary effect driving the dc transport properties in the paramagnetic orthorhombic state (i.e., the electronic nematic phase) is the anisotropy of the FS parameters (i.e., anisotropy in the Fermi velocity v_F, effective mass m^* and/or Fermi wave-vector k_F under an in-plane rotation of 90°) [57]. Early arguments based on band structure calculations similarly advocated that the transport anisotropy results from the FS anisotropy rather than the scattering rate one [71]. In this sense, as anticipated by previous elastoresistance measurements [50–52], the resistivity anisotropy directly connects to a thermodynamic

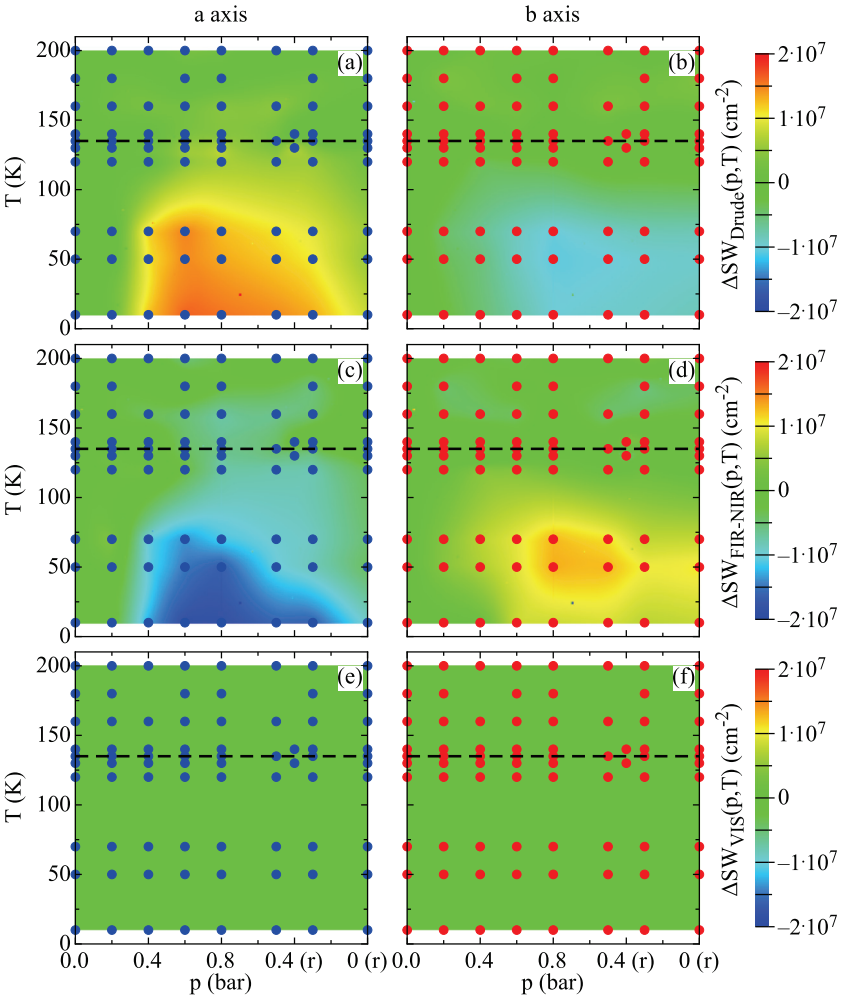

FIG. 5. Relative variation $[\Delta SW(p,T) = SW(p,T) - SW(0 \text{ bar},T)]$ of the squared oscillator-strengths with respect to the $p = 0$ bar situation (twinned sample) for selected fit components (Fig. 3) as a function of p and T along both axes: (a) and (b) Drude terms ($SW_{\text{Drude}} = \omega_{pN}^2 + \omega_{pB}^2$), (c) and (d) FIR-MIR-NIR ($SW_{\text{FIR-NIR}} = S_{\text{FIR}}^2 + S_{\text{MIR}}^2 + S_{\text{NIR}}^2$), and (e) and (f) visible-UV ranges ($SW_{\text{VIS}} = \sum_{j=1}^{2} S_j^2$). The dots indicate the fitted points for various combinations of p and T, which have been interpolated using a first-neighbor interpolation procedure to generate the color maps. The dashed line indicates the transition temperature $T_{s,N}$. Released pressures are denoted by "(r)."

quantity associated with the electronic nematic order, such as the difference in the occupancy of xz and yz orbitals in a two orbital model.

B. Optical spectral weight

It is of interest to elucidate how the spectral weight (SW) is redistributed in $\sigma_1(\omega)$ within different spectral ranges and for different combinations of p and T. We first exploit the Drude-Lorentz model, introduced in the previous section. The squared strength (ω_{pN}^2 and ω_{pB}^2 for the Drude terms and S^2 for HOs) of the fit components represents their own SW. We calculate the total SW encountered in the Drude terms ($SW_{\text{Drude}} = \omega_{pN}^2 + \omega_{pB}^2$), in the FIR, MIR and NIR HOs ($SW_{\text{FIR-NIR}} = S_{\text{FIR}}^2 + S_{\text{MIR}}^2 + S_{\text{NIR}}^2$), as well as in the visible up to the UV spectral range by adding the SW contribution of VIS-1 and VIS-2 HOs ($SW_{\text{VIS}} = \sum_{j=1}^{2} S_j^2$) (Fig. 3). Figure 5 displays $\Delta SW(p,T) = SW(p,T) - SW(0 \text{ bar},T)$ pertinent to the three selected spectral ranges (i.e., Drude terms, FIR-NIR, and VIS), defining the variation of SW within the fit components as a function of p and T with respect to the twinned case ($p = 0$ bar) along the a and b axes. We may anticipate that an important reshuffling of SW occurs at energy scales below 10^4 cm^{-1} ($\sim$1 eV, the typical energy scale of the VIS-1 HO) as soon as the sample gets progressively detwinned upon entering the orthorhombic, stripe-ordered phase. Indeed, there is an obvious enhancement of SW in the metallic components of $\sigma_1(\omega)$ and a depletion of SW in the FIR-NIR spectral range along the a axis, while the opposite is true along the b axis upon detwinning the specimen at $T \leqslant T_{s,N}$. SW essentially moves from MIR to the metallic component along the a axis and from the latter to the MIR spectral range along the b axis [57]. At frequencies pertinent to the visible and UV spectral range, no significant redistribution of SW is observed for both axes with respect to $p = 0$ bar at any T and p. Upon releasing p back to zero (i.e., the remanent phase), the SW imbalance with respect to the twinned case persists only at $T \ll T_{s,N}$. A further perspective on the accumulated SW within the fit components is given in Fig. 11 in Appendix.

An alternative view about the SW redistribution can be achieved by considering the integrated SW of the measured $\sigma_1(\omega)$ up to well defined cut-off energies (ω_c), given by

$$SW(p,T;\omega_c) = \int_0^{\omega_c} \sigma_1(\omega,p,T)d\omega. \qquad (2)$$

This model-independent quantity is related to the number of the effective carriers (normalized by their effective mass) contributing to the optical processes up to ω_c. Therefore, in the $\omega_c \to \infty$ limit, it is expected to merge to a constant value at all T and p, satisfying the f-sum rule [59].

Figure 6 displays the p and T dependence of $SW(\omega_c)$ along both axes for different ω_c, normalized by the corresponding

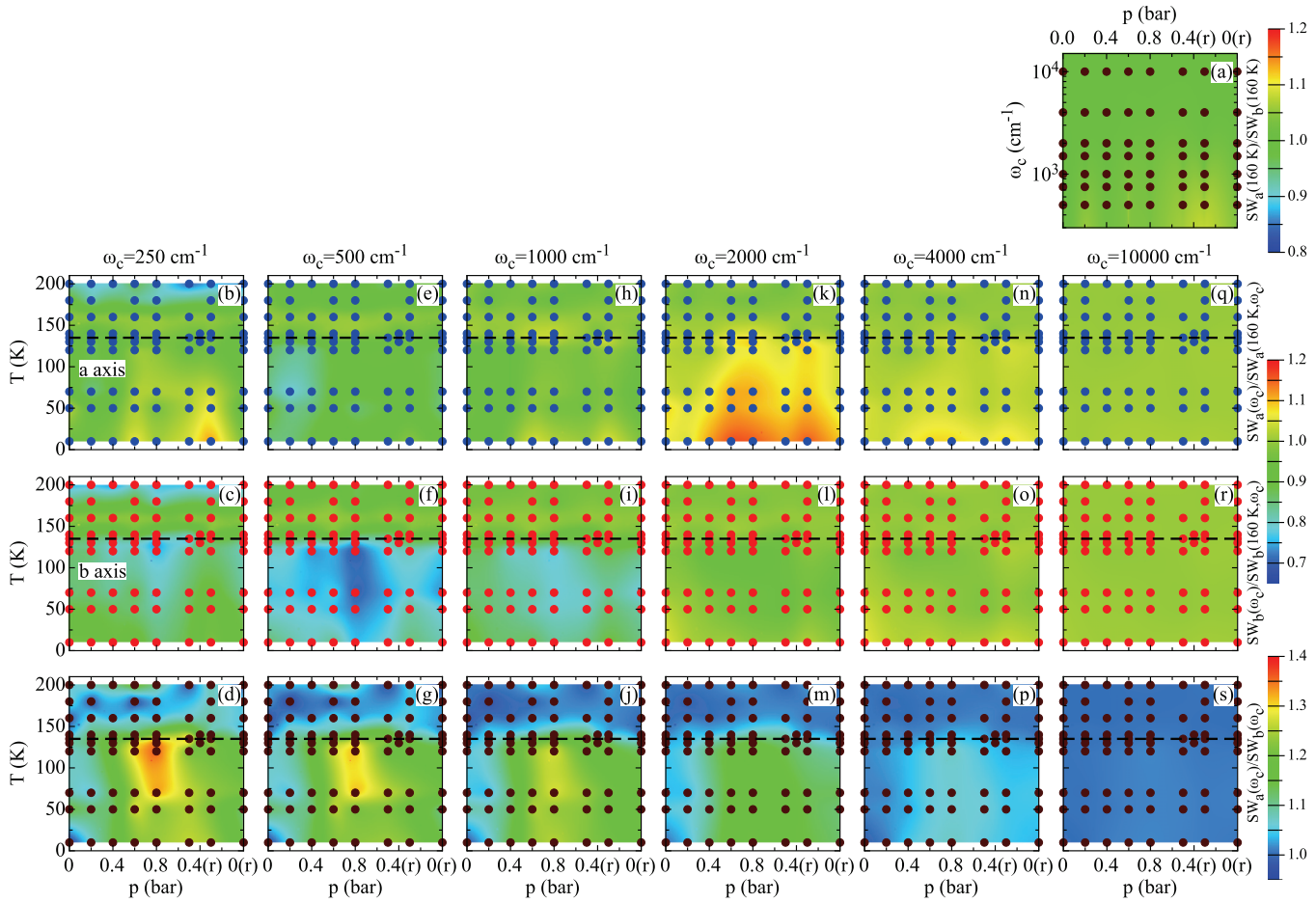

FIG. 6. (a) Ratio of the integrated spectral weight (SW) [Eq. (2)] between both axes at 160 K as a function of the cutoff frequency ω_c and applied uniaxial stress p, demonstrating that SW at this temperature is isotropic for all p and ω_c. This is further true at all $T \geqslant 160$ K. (b)–(s) Pressure and temperature dependence of SW, normalized by the corresponding quantity at 160 K for both a and b axes, as well as of the ratio SW_a/SW_b [72] estimated at the cutoff frequencies (b)–(d) $\omega_c = 250$, (e)–(g) 500, (h)–(j) 1000, (k)–(m) 2000, (n)–(p), 4000 and (q)–(s) 10000 cm^{-1}. The dots indicate the experimental (p,T) points, which have been interpolated using a first-neighbor interpolation procedure to generate the color maps. The dashed line indicates the transition temperature $T_{s,N}$. Released pressures are denoted by "(r)."

quantity at 160 K, a temperature below which the p-dependent, anisotropic optical response is observed (Figs. 1, 2, and 7). Indeed, SW for any ω_c at $T \geqslant 160$ K is isotropic [Fig. 6(a)] and turns out to be fully p-independent. In the same figure we also display the ratio $SW_a(\omega_c)/SW_b(\omega_c)$ at various ω_c, highlighting the p and T evolution of the anisotropy in the SW distribution [72]. We may remark with respect to 160 K a weak enhancement of SW for $\omega_c < 500$ cm^{-1} along the a axis [Figs. 6(b)–6(e)] versus a depletion of SW in the same spectral range along the b axis [Figs. 6(c)–6(f)], when entering the orthorhombic phase. The SW depletion along the b axis is particularly pronounced at $T < T_{s,N}$ for the fully detwinned specimen ($p \sim 0.8$ bar). Upon increasing ω_c there is a further enhancement of SW along the a axis, which piles up at $\omega_c < 2000$ cm^{-1} for $T \ll T_{s,N}$ and $p \geqslant 0.4$ bar [Fig. 6(k)], while along the b axis $\sigma_1(\omega)$ slowly recovers the spectral weight, removed for energies below 1000 cm^{-1} at $T < T_{s,N}$ and $p \sim 0.8$ bar [Figs. 6(i) and 6(l)]. At frequencies of about 4000 cm^{-1}, the SW overshoot along the a axis substantially vanishes and the SW along the b axis merges towards a constant value for all p and T [Figs. 6(n) and 6(o)]. The reshuffling of spectral weight thus occurs between the free-carriers contribution and the excitations in the FIR-MIR ranges, as a consequence of the SDW order. Along both axes and for $\omega_c \geqslant 10\,000$ cm^{-1} [Figs. 6(q) and 6(r)] there is a full recovery of SW at any T and uniaxial pressure, so that the integrated SW converges to its value at 160 K for the equivalent experimental conditions, in agreement with the f-sum rule expectation. What stated so far is then explicitly deployed in $SW_a(\omega_c)/SW_b(\omega_c)$ (third row of panels in Fig. 6). At $T \gg T_{s,N}$, the SW ratio between the a and b axis is close or equal to one at all p and for all cut-off frequencies. This is consistent with the isotropic character of the electronic structure in the high-temperature tetragonal phase. At $T \leqslant T_{s,N}$, more SW is encountered along the a axis than along the b axis, for any $\omega_c < 10\,000$ cm^{-1} and at uniaxial compressive stress exceeding 0.2 bar, as well as upon releasing p *in situ*, entering the remanent phase. We emphasize moreover the large anisotropy of SW at $p \sim 0.8$ bar (i.e., fully detwinned specimen) for 70 K $< T \leqslant T_{s,N}$ and for $\omega_c \sim 250$ cm^{-1}, which, combined with the anisotropy in the scattering rate (Fig. 4), accounts for the anisotropic dc transport

properties, specifically at the peak in $\rho(T)$ around $T_{s,N}$ (inset Fig. 3). The overall anisotropic behavior of the integrated SW is also supported by our phenomenological fit, based on the Drude-Lorentz model (Fig. 11 in the Appendix).

In summary, the SW depletion for $\omega_c \leqslant 1000$ cm^{-1} along the b axis and the piling up of SW up to energies $\omega_c \sim 2000$ cm^{-1} along the a axis, while one not being the consequence of the other, may be associated with typical fingerprints due to the FS gapping of the stripe-like SDW order, which is clearly exposed once the specimen is detwinned. Moreover, the metallic part of $\sigma_1(\omega)$ gets primarily suppressed at low T and for the single domain specimen along the b axis. The SW, achieved for any $\omega_c \geqslant 10\,000$ cm^{-1}, is constant at all T and for any p, and is identical among both axes, thus establishing $\omega \sim 1$ eV as a characteristic energy scale of the iron-pnictides, above which the optical response is fully isotropic as well as T-independent. It is worth pointing out, that from x-ray absorption spectroscopy data, one can determine the Hubbard $U \sim 2$ eV and the Hund's coupling $J \sim 0.8$ eV [73], which fall within the ranges of 2–5 eV and 0.6–0.9 eV for U and J, respectively, usually considered by LDA DMFT calculations [63,74–76]. Therefore, our SW analysis equally suggests the presence of correlation mechanism predominantly due to Hund's coupling, confirming previous conjecture based on data for twinned samples [69,77] and further supporting theoretical approaches based on sizable correlation effects [78].

V. CONCLUSIONS

Our reflectivity data of a representative parent compound of the iron-pnictide superconductors, collected over a broad spectral range, and the analysis of the extracted optical conductivity allow shedding light on the anisotropic electrodynamic response across the structural phase transition and as a function of the external symmetry breaking field, exerted here by a tunable uniaxial compressive stress. The well-known anisotropy related to the electronic nematic state at energy scales far away from the Fermi surface [54,55] is now complemented by a remarkable anisotropy of the low frequency charge dynamics. Our optical investigation reveals that in the paramagnetic tetragonal phase the induced dc resistivity anisotropy of strained samples is almost exclusively due to stress-induced changes in the Drude spectral weight rather than in the scattering rate. This result definitively establishes the anisotropy of the Fermi surface parameters as the primary effect driving the dc transport properties in the electronic nematic state of this material. Our work now resolves a long-standing issue of fundamental importance; even though impurity scattering can affect the transport anisotropy in subtle ways, it seems to have at best only limited relevance in the electronic nematic phase. Even though the multiband nature of the iron-pnictides hampers precisely tracking the behavior of each single band crossing the Fermi level, our findings further call for a large anisotropy of the resulting conduction bands upon detwinning the specimen. In this context, we have shown that the related reshuffling of spectral weight in $\sigma_1(\omega)$ across the structural phase transition occurs within 1 eV from the Fermi level, thus favoring Hund's coupling as driving correlation effect.

We shall finally link our optical findings to some selected ideas from the vast theoretical work present in the literature, also offering an opportunity for an outlook about future activities. One of the major debated issues is about the role played by orbital and magnetic order, spin fluctuations and impurity scattering in defining the underlying physics of this class of materials, particularly in terms of their anisotropic physical properties. We start our theoretical survey by quoting the calculation of the x-ray absorption linear dichroism by Chen *et al.* [4], who first anticipated the importance of orbital order. The orbital order is represented by an energy splitting between the two otherwise degenerate d_{xz} and d_{yz} orbitals. After Ref. [4], the FS reconstruction below T_N, as evinced in angle-resolved photoemission spectroscopy experiments [34,35], may be understood when the SDW field is further accompanied by an orbital polarization, consistent with the optical dichroism shown in Fig. 7 in the Appendix. The optical conductivity was then explicitly calculated by Lv and Phillips [6], within the five-orbital Hubbard model using a self-consistent mean-field theory. They state that the inclusion of both orbital and magnetic order is essential. The orbital nematic order is well imaged by the optical anisotropy discovered at MIR frequencies (Figs. 2 and 7) and also causes the Drude weight anisotropy, as observed in our experiment [57]. Furthermore, the magnetic order, setting in at low temperatures, theoretically leads to the reshuffling of spectral weight, which induces the enhancement/depletion of $\sigma_1(\omega)$ in its metallic part along the a/b axis, respectively, and to the opening of a gap as well as the emergence of anisotropic peaks in $\sigma_1(\omega)$ [6], mimicking pretty much precisely the overall trend of the measured optical conductivity at low T (Figs. 2 and 7). The anisotropic Drude weight of the itinerant charge carriers was also considered in the attempt by Liang *et al.* in order to explain the origin of the dc anisotropy [79]. They develop a spin-fermion model, within a Monte Carlo simulation, in which they explicitly include a symmetry breaking term due to the strain effects. All major fingerprints of the anisotropic dc transport of $BaFe_2As_2$, like the anisotropic peak in $\rho(T)$ around T_N, are reproduced, which qualitatively appears related to short-range spin order and concomitant FS orbital order [79].

The significance of orbital order is, however, controversial. For instance, Sugimoto *et al.* claim that at least below T_N the AFM ordering is enough to explain the discovered optical anisotropy, with no need to introduce any orbital order effect [64]. Valenzuela *et al.* [80] further point out that instead of orbital order the anisotropy of the Fermi velocity, tightly related to the anisotropic topology of FS in a multiorbital system, drives the anisotropy in the Drude weight and thus in the metallic part of the optical conductivity (Figs. 2 and 7). They even claim that orbital order would lead to an opposite trend in the anisotropy of the Drude weight than observed experimentally (Fig. 11) [80]. The same group also argues that the Drude weight anisotropy in the magnetic state is sensitive to small changes in the lattice structure, particularly the Fe-As angle [67], and proposes [68] that electronic interactions lead to low-energy interband transitions, as anticipated by Ref. [66], influencing the Drude response in a nontrivial manner.

In the approaches mentioned so far, the impact of the charge scattering was neglected or at most it was included as a constant parameter into the calculations. However, we

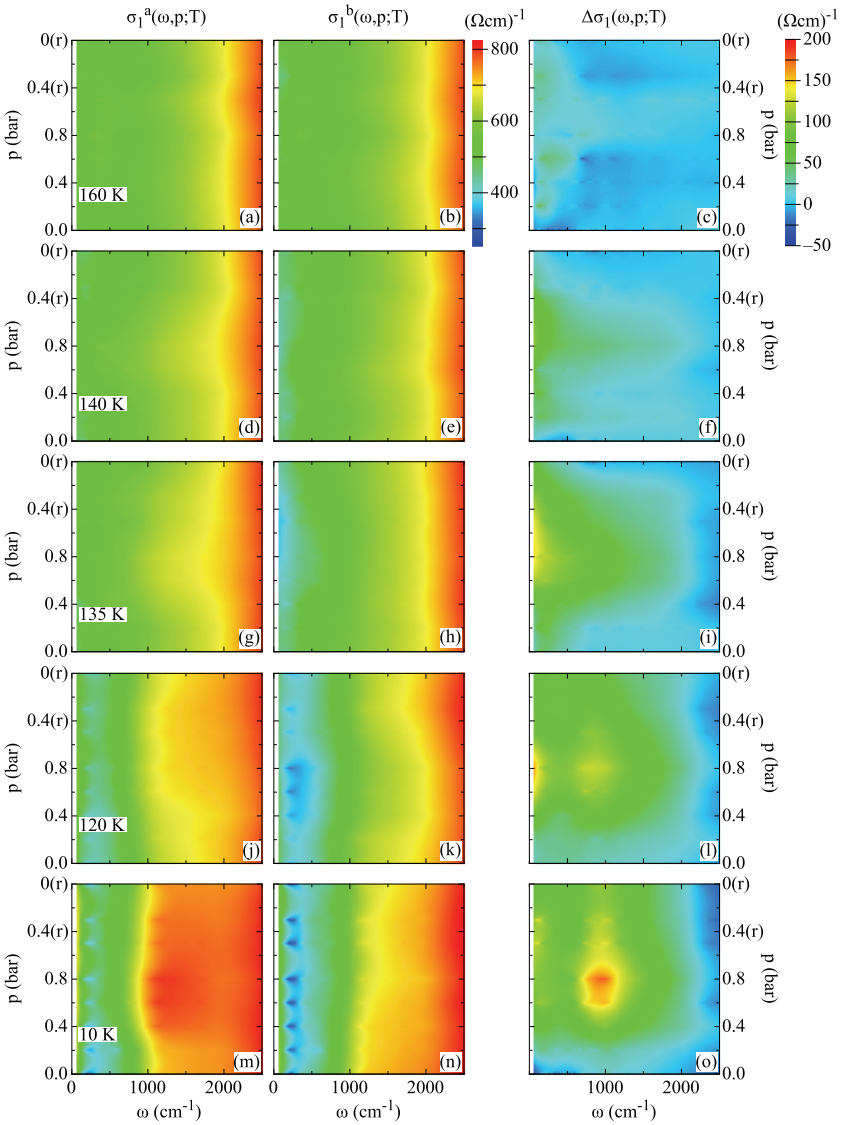

FIG. 7. Color maps of the p dependence of the real part $\sigma_1(\omega)$ of the optical conductivity along the a and b axis [57] as well as of $\Delta\sigma_1(\omega, p; T) = \sigma_1^a(\omega, p; T) - \sigma_1^b(\omega, p; T)$ up to 2500 cm^{-1} at (a)–(c) 160, (d)–(f) 140, (g)–(i) 135, (j)–(l) 120, and (m)–(o) 10 K. Data have been interpolated using a first-neighbor interpolation procedure to generate the color maps. Released pressures are denoted by "(r)."

have shown that the scattering rate of the itinerant charge carriers is also an important quantity since it may change as a function of temperature and degree of sample detwinning [Figs. 4(c), 4(d), 4(g), and 4(h)] [57]. Several dedicated theoretical work recently reproduce the dc transport anisotropy within scenarios based on anisotropic scattering with spin fluctuations [81–86].

For instance, Fernandes *et al.* [82] applied a model, restricted to $T \geqslant T_N$, based on the Ising-nematic order which causes an anisotropy in the magnetic fluctuations, thus inducing an anisotropy in the resistivity in agreement with the experiment. Breitkreiz *et al.* emphasize the role of the spin-fluctuation scattering strength in controlling the size of the FS areas, which contribute to the resistivity anisotropy, but neglect the effect of FS distortion due to the splitting of the iron d_{zx} and d_{yz} orbitals [83].

Gastiasoro *et al.* first considered nematic defects in the ordered phase (i.e., $T < T_s$), which consist of elongated dimer-like structures resulting from nonmagnetic impurity [84]. The nematic defect structures (i.e., nematogens), which are aligned along the AFM a axis, turn out to scatter more the carriers along the FM b axis and cause the resistivity anisotropy. In a sequel work, Gastiasoro *et al.* studied the impact of emergent nematogen defect states above T_N, claiming the unusual role played by impurities in these systems with strong spin fluctuations near a magnetic transition [85]. The impact of nematogens is supposed to rise upon doping, thus enhancing the dc anisotropy. Liang *et al.* further elaborate this issue and propose, based on a Monte Carlo simulation within the three-orbital spin fermion model with lattice degrees of freedom, that the fast reduction with doping of the Néel T_N and the structural T_s transition temperatures, and the concomitant stabilization of a robust nematic state, are primarily controlled by the magnetic dilution associated with the in-plane isotropic disorder introduced by Fe substitution [87].

Finally, Wang *et al.* address the effect of impurity scattering within a simple two-band model of a dirty SDW metal, which explains the origin of the dc transport anisotropy with the collapse in the scattering rate due to the decrease in scattering phase space upon partial gapping the FS [86]. Therefore the suppressed scattering rate overcompensates the loss of carriers related to the SDW transition. The dc anisotropy is then affected by the Lifshitz transition following the Fermi surface reconstruction upon magnetic ordering (i.e.,

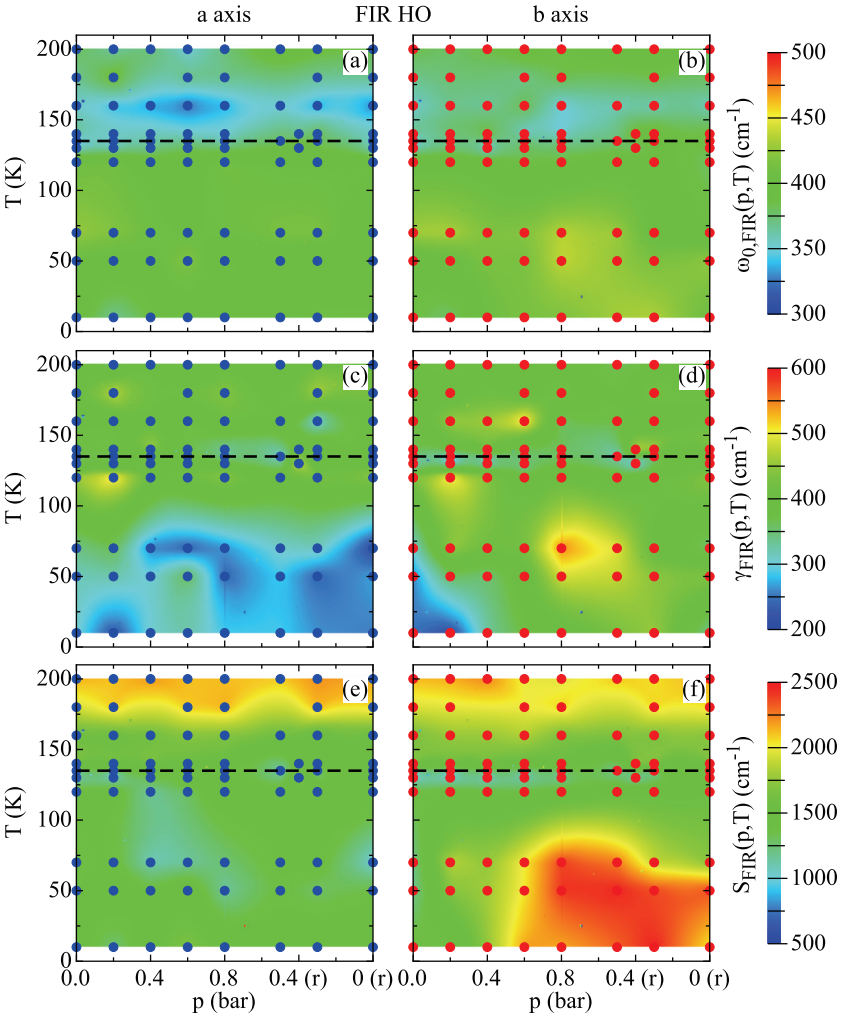

FIG. 8. Pressure and temperature dependence of the fit parameters for the FIR HO (see also Supplemental Material of Ref. [57]). The panels show the peak frequency ω_0 [(a) and (b)], the width γ [(c) and (d)] and the strength S [(e) and (f)] for the a and b axis, respectively. The dots indicate the fitted (p,T) points, which have been interpolated using a first-neighbor interpolation procedure to generate the color maps. The dashed line indicates the transition temperature $T_{s,N}$. Released pressures are denoted by "(r)."

disappearing of Fermi pockets due to the increasing SDW potential) [86].

Even though these latter scenarios [84–87] may catch the overall features of the experimental dc transport properties, they do not match with our findings, which hint to an opposite anisotropy of the intrinsic Drude parameters. In order to solve and clarify that discrepancy, a central task would be to figure out which scattering mechanisms dominate in optical experiments. This could indicate possible theoretical avenues in order to shed light on the interplay between scattering rate and Drude weight, as shown by our work. This is still a challenging theoretical endeavor, which will keep us busy for a long time to come.

Note added in proof. Recently, we came across the work by Schütt *et al.* [88], who address the impact of spin fluctuations on the anisotropic optical conductivity. Spin fluctuations induce the electronic Fermi velocity renormalization causing opposite changes in the effective scattering rate and plasma frequencies anisotropies, in broad agreement with conclusions drawn from our study.

ACKNOWLEDGMENTS

The authors wish to thank E. Bascones, R. Fernandes, B. Valenzuela, A. Chubukov, P. Hirschfeld, B. Andersen, M. Gastiasoro, W. Ku, Q. Si, E.W. Carlson, M. Sigrist, S. Kivelson, M. Dressel, D.N. Basov, R. Prozorov, and D. Lu for fruitful discussions. This work was supported by the Swiss National Science Foundation (SNSF). Work at Stanford University was supported by the Department of Energy, Office of Basic Energy Sciences under Contract DE-AC02-76SF00515. L.D. acknowledges the hospitality at KITP (UC Santa Barbara) within the IRONIC14 Workshop, where part of this paper was conceived.

APPENDIX

1. Optical conductivity and dichroism

In addition to the data displayed in Fig. 2, we show in the left and central panels of Fig. 7 the p dependence of the real part $\sigma_1(\omega)$ of the optical conductivity in the FIR-MIR spectral range ($\omega \sim 60$–2500 cm^{-1}) at selected temperatures above, at and below $T_{s,N}$ [57]. The characteristic fingerprints pertinent to the p evolution of the optical anisotropy across the structural transition at low frequencies are the FIR depletion and the narrowing of the metallic contribution mainly along the b axis and the strong enhancement of the MIR absorption feature (i.e., at about 1300 cm^{-1}) primarily along the a axis with decreasing temperature below $T_{s,N}$ and upon fully detwinning the sample. Overall, one can safely state that the lower is T

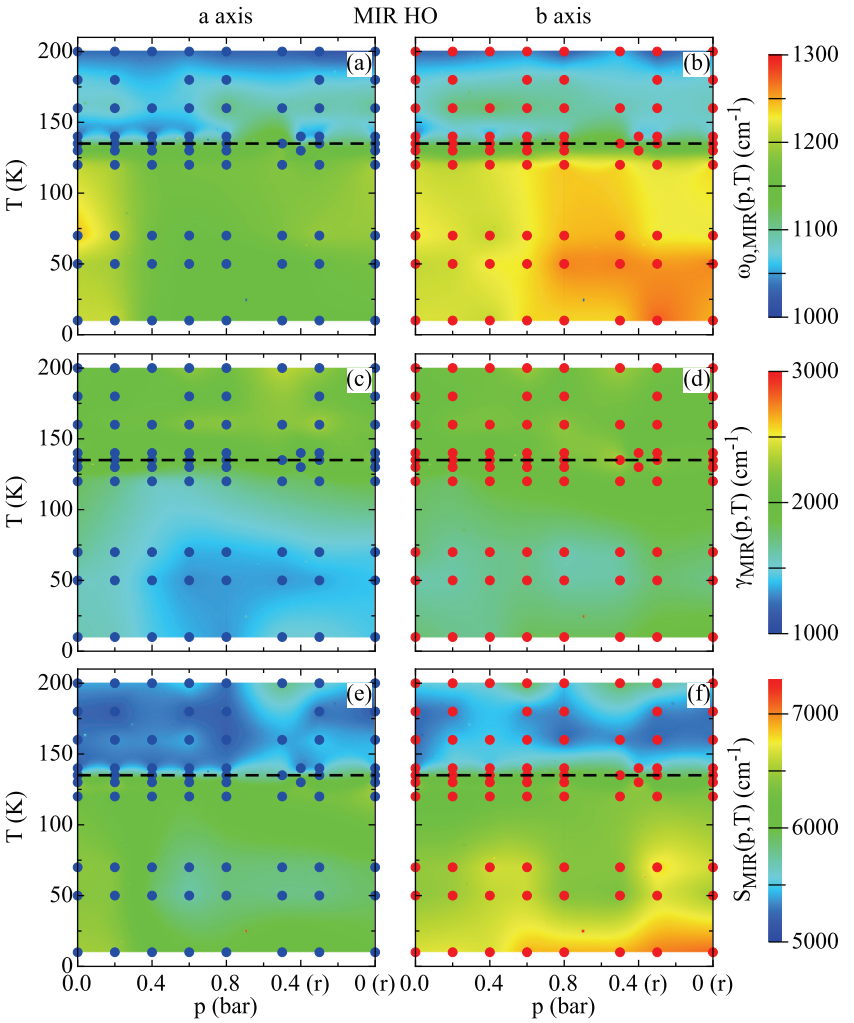

FIG. 9. Pressure and temperature dependence of the fit parameters for the MIR HO (see also Supplemental Material of Ref. [57]). The panels show the peak frequency ω_0 [(a) and (b)], the width γ [(c) and (d)], and the strength S [(e) and (f)] for the a and b axes, respectively. The dots indicate the fitted (p,T) points, which have been interpolated using a first-neighbor interpolation procedure to generate the color maps. The dashed line indicates the transition temperature $T_{s,N}$. Released pressures are denoted by "(r)."

and the more single-domain like is the specimen, the more enhanced is $\sigma_1(\omega)$ along the a axis with respect to the b axis for $\omega \leqslant 2000\,\mathrm{cm}^{-1}$. Our observations are readily reinforced by the quantity $\Delta\sigma_1(\omega,p;T) = \sigma_1^a(\omega,p;T) - \sigma_1^b(\omega,p;T)$ (right panels of Fig. 7), which may be considered as an alternative definition of the dichroism, imaging the anisotropy of the optical response.

2. Harmonic oscillators in the Drude-Lorentz fit

We display here the fit parameters of the HOs, introduced in Fig. 3 in the main paper, which, together with the parameters of the Drude terms (Fig. 4), well describe the optical response of the title compound. Figures 8, 9, and 10 show the p and T dependence of the peak frequency ω_0 [(a) and (b)], the width γ [(c) and (d)], and the oscillator strength S [(e) and (f)] of the FIR, MIR and NIR HOs. Table I summarizes the same fit parameters for the two visible (VIS) HOs, which turn out to be totally p- and T-independent [$j = 1, 2$ in Eq. (1)].

We shall just point out a few characteristic features for each HO (see also Supplemental Material of Ref. [57]). For the FIR HO (Fig. 8), ω_0 is almost p- and T-independent and is totally isotropic between both axes. The anisotropy of its width develops because of the pronounced narrowing at $T \ll T_{s,N}$ along the a axis for $p \sim 0.8$ bar and upon releasing p back to zero. The HO strength gets overall depleted with decreasing T below 160 K for both axes. The anisotropy of this parameter is mainly due to its subsequent strong enhancement at $T \ll T_{s,N}$ along the b axis for $p \geqslant 0.6$ bar and upon releasing p back to zero.

The peak frequency of the MIR HO (Fig. 9) is enhanced when crossing $T_{s,N}$ and is anisotropic below $T_{s,N}$, since the frequency up-shift is pretty remarkable and stronger along the b axis than along the a axis. On the other hand, for $p \sim 0.8$ bar and upon releasing p back to zero at $T \ll T_{s,N}$, there is a narrowing of the MIR HO along the a axis. The HO strength gets predominately enhanced in the orthorhombic phase and particularly along the b axis for $p \geqslant 0.4$ bar as well as upon releasing p back to zero at $T \ll T_{s,N}$.

As far as the NIR HO is concerned (Fig. 10), the peak frequency shifts in an isotropic fashion to lower values at $T \leqslant$

TABLE I. Peak-frequency (ω_{0j}), strength (S_j) and width (γ_j) of the two p- and T-independent HOs [Eq. (1)] in the visible-UV spectral range (Fig. 3).

HO	ω_{0j} (cm^{-1})	S_j (cm^{-1})	γ_j (cm^{-1})
VIS-1	17 000	26 000	22 000
VIS-2	29 000	15 000	18 000

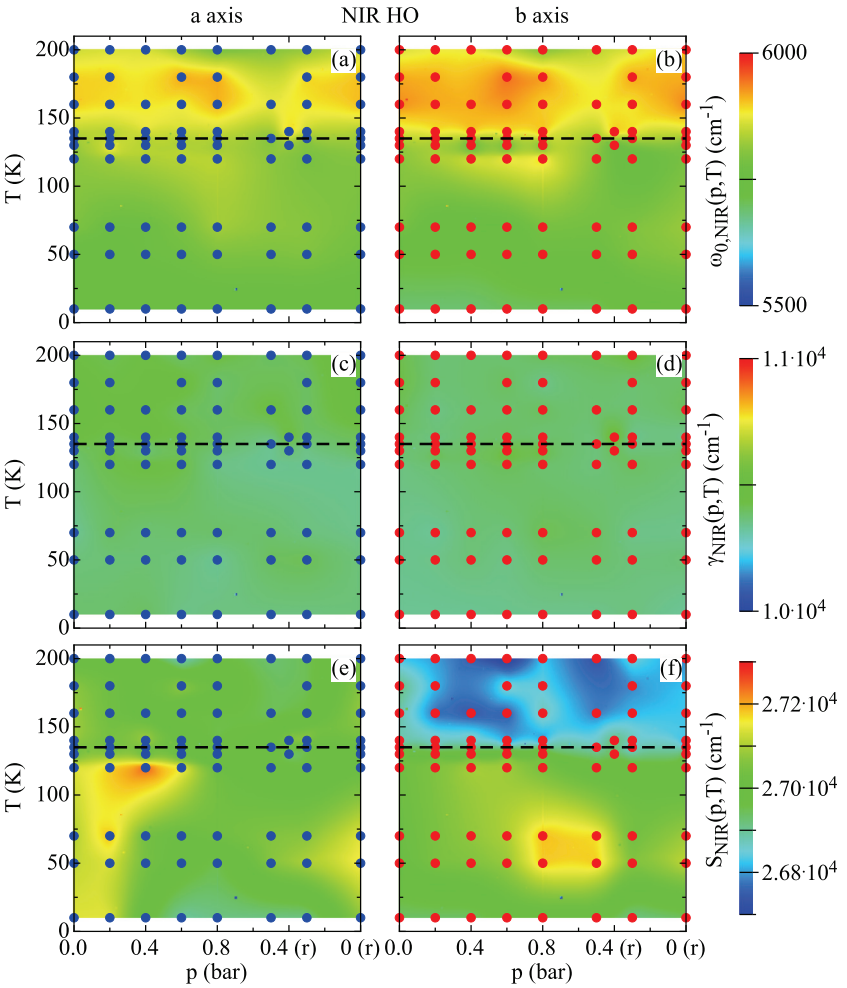

FIG. 10. Pressure and temperature dependence of the fit parameters for the NIR HO (see also Supplemental Material of Ref. [57]). The panels show the peak frequency ω_0 [(a) and (b)], the width γ [(c) and (d)], and the strength S [(e) and (f)] for the a and b axes, respectively. The dots indicate the fitted (p,T) points, which have been interpolated using a first-neighbor interpolation procedure to generate the color maps. The dashed line indicates the transition temperature $T_{s,N}$. Released pressures are denoted by "(r)."

$T_{s,N}$ for all p, while its width remains constant for both crystallographic directions. The HO strength is slightly enhanced for $p \leqslant 0.2$ bar along the a axis at $T \leqslant T_{s,N}$, prior recovering a T-independent value upon applying p, as well as releasing it. Along the b axis, the strength in the orthorhombic phase is enhanced for all p, somehow in a stronger manner for 50 $K \leqslant T \leqslant 70$ K close to saturation (i.e., at 0.8 and released 0.5 bar).

Finally, we shall briefly comment on the IR-active phonon mode (OP in Fig. 3), which is only detected along the b axis at $T \leqslant T_{s,N}$, while it disappears above $T_{s,N}$ because of the screening due to the metallic components of $\sigma_1(\omega)$ (see also main paper). At $T \leqslant T_{s,N}$, the phonon fit parameters are almost p-independent so that the peak frequency is at about 260 cm^{-1}, its width lies between 3 to 10 cm^{-1} and the strength amounts to approximately 100 cm^{-1}. These latter values are very much consistent with the experimental finding at low temperatures of Ref. [69]. The OP contribution to the fit procedure is however quite negligible and does not affect its quality.

3. Spectral weight analysis from the Drude-Lorentz fit

At this stage it is instructive to perform a spectral weight (SW) analysis by deploying its evolution within the various fit components shaping $\sigma_1(\omega)$ along both crystallographic axes, which is complementary to the analysis of its relative reshuffling in the fitted spectral ranges, shown in Fig. 5. The panels (a)–(d) and (e)–(h) of Fig. 11 show the p and T dependence of the accumulated spectral weight $\sum_{i=0}^{j} SW_i$ for both axes, normalized by the same quantity at 160 K, where SW_i may be the squared plasma frequency $\omega^2_{pN/B}$ of the narrow and broad Drude term and/or the squared HO strength S^2. Figures 11(i)–11(l) display the ratio $\sum_{i=0}^{j} SW_i^a / \sum_{i=0}^{j} SW_i^b$, highlighting the anisotropy of the accumulated SW. Therefore the first column accounts for the accumulated SW into the Drude terms ($j = 1$: $i = 0$, narrow and $i = 1$, broad), while the remaining columns report it by progressively adding SW of the FIR ($j = 2$), MIR ($j = 3$), and NIR ($j = 4$) HO. This analysis backs up and overall confirms what stated in the paper upon discussing the model independent, integrated SW [Eq. (2) and Fig. 6]. The major reshuffling of SW occurs at energy scales pertinent to the metallic and FIR-MIR contributions for each polarization. At energy scales shaped by the NIR contribution the accumulated SW at 160 K is recovered at any p and T, satisfying the f-sum rule. In other words, the accumulated SW gets yet depleted at $T \leqslant T_{s,N}$ for energies below 1 eV, though this depletion is more substantial along the b axis than along the a axis for detwinned specimens as well as in the remanent state. Conversely, the anisotropy of SW [Figs. 11(i)–11(l)] reflects the larger accumulated weight encountered in $\sigma_1(\omega)$ below 1 eV along the a axis with respect to the b axis when $T \leqslant T_{s,N}$ and the specimen is fully detwinned. The largest anisotropy in the accumulated SW is principally recognized in the spectral range associated

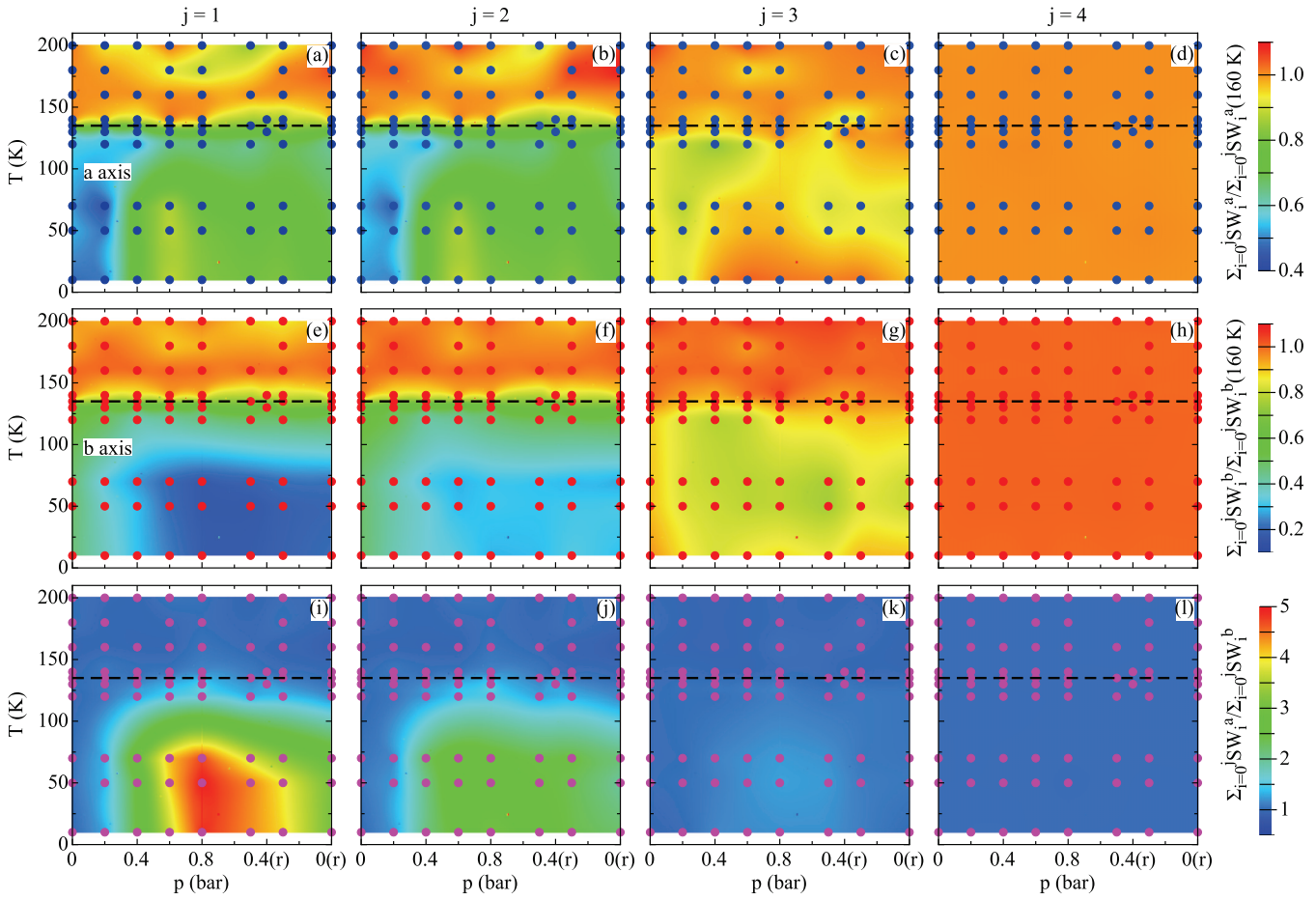

FIG. 11. Pressure and temperature dependence of the accumulated SW within the Drude-Lorentz fit components. The panels in the upper two rows display $\sum_{i=0}^{j} SW_i$ for the a (a)–(d) and b axis (e)–(h), normalized by the same quantity at 160 K. SW_i may be the squared plasma frequency $\omega^2_{pN/B}$ of the narrow and broad Drude term and/or the squared HO strength S^2. The third row (i-l) displays the ratio $\sum_{i=0}^{j} SW_i^a / \sum_{i=0}^{j} SW_i^b$, highlighting the anisotropy of the accumulated SW upon progressively adding the various fit components ($i = 0$: narrow and $i = 1$: broad Drude terms, $i = 2$: FIR, $i = 3$: MIR and $i = 4$: NIR HO). The dots indicate the fitted (p, T) points, which have been interpolated using a first-neighbor interpolation procedure to generate the color maps. The dashed line indicates the transition temperature $T_{s,N}$. Released pressures are denoted by "(r)."

with the metallic components, while it persists into the FIR and weakens considerably up to the MIR energy interval at saturation and upon slightly releasing p. The SW anisotropy then fully disappears into the NIR energy range for any T and p, so that the accumulated SW is here identical for both axes.

[1] I. R. Fisher, L. Degiorgi, and Z. X. Shen, In-plane electronic anisotropy of underdoped '122' Fe-arsenide superconductors revealed by measurements of detwinned single crystals, Rep. Prog. Phys. **74**, 124506 (2011) and references therein.

[2] M. A. Tanatar, A. Kreyssig, S. Nandi, N. Ni, S. L. Bud'ko, P. C. Canfield, A. I. Goldman, and R. Prozorov, Direct imaging of the structural domains in the iron pnictides AFe_2As_2 (A=Ca, Sr, Ba), Phys. Rev. B **79**, 180508(R) (2009).

[3] C.-C. Lee, W.-G. Yin, and W. Ku, Ferro-Orbital Order and Strong Magnetic Anisotropy in the Parent Compounds of Iron-Pnictide Superconductors, Phys. Rev. Lett. **103**, 267001 (2009).

[4] C.-C. Chen, J. Maciejko, A. P. Sorini, B. Moritz, R. R. P. Singh, and T. P. Devereaux, Orbital order and spontaneous orthorhombicity in iron pnictides, Phys. Rev. B **82**, 100504(R) (2010).

[5] W. Lv, F. Krüger, and P. Phillips, Orbital ordering and unfrustrated $(\pi, 0)$ magnetism from degenerate double exchange in the iron pnictides, Phys. Rev. B **82**, 045125 (2010).

[6] W. Lv and P. Phillips, Orbitally and magnetically induced anisotropy in iron-based superconductors, Phys. Rev. B **84**, 174512 (2011).

[7] X. Zhang and E. Dagotto, Anisotropy of the optical conductivity of a pnictide superconductor from the undoped three-orbital Hubbard model, Phys. Rev. B **84**, 132505 (2011).

[8] Z. Wang and A. H. Nevidomskyy, Orbital nematic order and interplay with magnetism in the two-orbital Hubbard model, J. Phys.: Condens. Matter **27**, 225602 (2015).

[9] R. M. Fernandes and A. J. Millis, Nematicity as a Probe of Superconducting Pairing in Iron-Based Superconductors, Phys. Rev. Lett. **111**, 127001 (2013).

[10] C. Fang, H. Yao, W.-F. Tsai, J. P. Hu, and S. A. Kivelson, Theory of electron nematic order in LaFeAsO, Phys. Rev. B **77**, 224509 (2008).

[11] C. Xu, M. Müller, and S. Sachdev, Ising and spin orders in the iron-based superconductors, Phys. Rev. B **78**, 020501(R) (2008).

[12] R. M. Fernandes, A. V. Chubukov, J. Knolle, I. Eremin, and J. Schmalian, Preemptive nematic order, pseudogap, and orbital order in the iron pnictides, Phys. Rev. B **85**, 024534 (2012); **85**, 109901(E) (2012).

[13] R. M. Fernandes, A. V. Chubukov, and J. Schmalian, What drives nematic order in iron-based superconductors? Nat. Phys. **10**, 97 (2014).

[14] E. W. Carlson and K. A. Dahmen, Using disorder to detect locally ordered electron nematics via hysteresis, Nat. Commun. **2**, 379 (2011).

[15] J.-H. Chu, J. G. Analytis, D. Press, K. De Greve, T. D. Ladd, Y. Yamamoto, and I. R. Fisher, In-plane electronic anisotropy in underdoped $Ba(Fe_{1-x}Co_x)_2As_2$ revealed by partial detwinning in a magnetic field, Phys. Rev. B **81**, 214502 (2010).

[16] J. P. C. Ruff, J.-H. Chu, H.-H. Kuo, R. K. Das, H. Nojiri, I. R. Fisher, and Z. Islam, Susceptibility Anisotropy in an Iron Arsenide Superconductor Revealed by X-ray Diffraction in Pulsed Magnetic Fields, Phys. Rev. Lett. **109**, 027004 (2012).

[17] J.-H. Chu, J. G. Analytis, K. De Greve, P. L. McMahon, Z. Islam, Y. Yamamoto, and I. R. Fisher, In-plane resistivity anisotropy in an underdoped iron arsenide superconductor, Science **329**, 824 (2010).

[18] E. C. Blomberg, M. A. Tanatar, A. Kreyssig, N. Ni, A. Thaler, Rongwei Hu, S. L. Bud'ko, P. C. Canfield, A. I. Goldman, and R. Prozorov, In-plane anisotropy of electrical resistivity in strain-detwinned $SrFe_2As_2$, Phys. Rev. B **83**, 134505 (2011).

[19] E. C. Blomberg, A. Kreyssig, M. A. Tanatar, R. M. Fernandes, M. G. Kim, A. Thaler, J. Schmalian, S. L. Bud'ko, P. C. Canfield, A. I. Goldman, and R. Prozorov, Effect of tensile stress on the in-plane resistivity anisotropy in $BaFe_2As_2$, Phys. Rev. B **85**, 144509 (2012).

[20] S. Ishida, M. Nakajima, T. Liang, K. Kihou, C. H. Lee, A. Iyo, H. Eisaki, T. Kakeshita, Y. Tomioka, T. Ito, and S. Uchida, Anisotropy of the In-Plane Resistivity of Underdoped $Ba(Fe_{1-x}Co_x)_2As_2$ Superconductors Induced by Impurity Scattering in the Antiferromagnetic Orthorhombic Phase, Phys. Rev. Lett. **110**, 207001 (2013).

[21] A. F. Wang, J. J. Ying, X. G. Luo, Y. J. Yan, D. Y. Liu, Z. J. Xiang, P. Cheng, G. J. Ye, L. J. Zou, Z. Sun, and X. H. Chen, A crossover in the phase diagram of $NaFe_{1-x}Co_xAs$ determined by electronic transport measurements, New J. Phys. **15**, 043048 (2013).

[22] J. J. Ying, X. F. Wang, T. Wu, Z. J. Xiang, R. H. Liu, Y. J. Yan, A. F. Wang, M. Zhang, G. J. Ye, P. Cheng, J. P. Hu, and X. H. Chen, Measurements of the Anisotropic In-Plane Resistivity of Underdoped FeAs-Based Pnictide Superconductors, Phys. Rev. Lett. **107**, 067001 (2011).

[23] E. C. Blomberg, M. A. Tanatar, R. M. Fernandes, I. I. Mazin, B. Shen, H.-H. Wen, M. D. Johannes, J. Schmalian, and R. Prozorov, Sign-reversal of the in-plane resistivity anisotropy in hole-doped iron pnictides, Nat. Commun. **4**, 1914 (2013).

[24] S. Jiang, H. S. Jeevan, J. Dong, and P. Gegenwart, Thermopower as a Sensitive Probe of Electronic Nematicity in Iron Pnictides, Phys. Rev. Lett. **110**, 067001 (2013).

[25] R. M. Fernandes, L. H. VanBebber, S. Bhattacharya, P. Chandra, V. Keppens, D. Mandrus, M. A. McGuire, B. C. Sales, A. S. Sefat, and J. Schmalian, Effects of Nematic Fluctuations on the Elastic Properties of Iron Arsenide Superconductors, Phys. Rev. Lett. **105**, 157003 (2010).

[26] A. E. Böhmer, P. Burger, F. Hardy, T. Wolf, P. Schweiss, R. Fromknecht, M. Reinecker, W. Schranz, and C. Meingast, Nematic Susceptibility of Hole-Doped and Electron-Doped $BaFe_2As_2$ Iron-Based Superconductors from Shear Modulus Measurements, Phys. Rev. Lett. **112**, 047001 (2014).

[27] R. M. Fernandes, A. E. Böhmer, C. Meingast, and J. Schmalian, Scaling between Magnetic and Lattice Fluctuations in Iron Pnictide Superconductors, Phys. Rev. Lett. **111**, 137001 (2013).

[28] S.-H. Baek, D. V. Efremov, J. M. Ok, J. S. Kim, J. van den Brink, and B. Büchner, Orbital-driven nematicity in FeSe, Nat. Mater. **14**, 210 (2015).

[29] C. Dhital, Z. Yamani, W. Tian, J. Zeretsky, A. S. Sefat, Z. Wang, R. J. Birgeneau, and S. D. Wilson, Effect of Uniaxial Strain on the Structural and Magnetic Phase Transitions in $BaFe_2As_2$, Phys. Rev. Lett. **108**, 087001 (2012).

[30] L. W. Harriger, H. Q. Luo, M. S. Liu, C. Frost, J. P. Hu, M. R. Norman, and P. Dai, Nematic spin fluid in the tetragonal phase of $BaFe_2As_2$, Phys. Rev. B **84**, 054544 (2011).

[31] Y. Song, S. V. Carr, X. Lu, C. Zhang, Z. C. Sims, N. F. Luttrell, S. Chi, Y. Zhao, J. W. Lynn, and P. Dai, Uniaxial pressure effect on structural and magnetic phase transitions in NaFeAs and its comparison with as-grown and annealed $BaFe_2As_2$, Phys. Rev. B **87**, 184511 (2013).

[32] S. Avci, O. Chmaissem, J. M. Allred, S. Rosenkranz, I. Eremin, A. V. Chubukov, D. E. Bugaris, D. Y. Chung, M. G. Kanatzidis, J.-P. Castellan, J. A. Schlueter, H. Claus, D. D. Khalyavin, P. Manuel, A. Daoud-Aladine, and R. Osborn, Magnetically driven suppression of nematic order in an iron-based superconductor, Nat. Commun. **5**, 3845 (2014).

[33] X. Lu, J. T. Park, R. Zhang, H. Luo, A. H. Nevidomskyy, Q. Si, and P. Dai, Nematic spin correlations in the tetragonal state of uniaxial-strained $BaFe_{2-x}Ni_xAs_2$, Science **345**, 657 (2014).

[34] M. Yi, D. Lu, J.-H. Chu, J. G. Analytis, A. P. Sorini, A. F. Kemper, B. Moritz, S.-K. Mo, R. G. Moore, M. Hashimoto, W.-S. Lee, Z. Hussain, T. P. Devereaux, I. R. Fisher, and Z.-X. Shen, Symmetry-breaking orbital anisotropy observed for detwinned $Ba(Fe_{1-x}Co_x)_2As_2$ above the spin density wave transition, Proc. Natl. Acad. Sci. USA **108**, 6878 (2011).

[35] M. Yi, D. H. Lu, R. G. Moore, K. Kihou, C.-H. Lee, A. Iyo, H. Eisaki, T. Yoshida, A. Fujimori, and Z.-X. Shen, Electronic reconstruction through the structural and magnetic transitions in detwinned NaFeAs, New J. Phys. **14**, 073019 (2012).

[36] Q. Wang, Z. Sun, E. Rotenberg, F. Ronning, E. D. Bauer, H. Lin, R. S. Markiewicz, M. Lindroos, B. Barbiellini, A. Bansil, and D. S. Dessau, Symmetry-broken electronic structure and uniaxial Fermi surface nesting of untwinned $CaFe_2As_2$, Phys. Rev. B **88**, 235125 (2013).

[37] K. Nakayama, Y. Miyata, G. N. Phan, T. Sato, Y. Tanabe, T. Urata, K. Tanigaki, and T. Takahashi, Reconstruction of Band Structure Induced by Electronic Nematicity in an FeSe Superconductor, Phys. Rev. Lett. **113**, 237001 (2014).

[38] T.-M. Chuang, M. P. Allan, J. Lee, Y. Xie, N. Ni, S. L. Bud'ko, G. S. Boebinger, P. C. Canfield, and J. C. Davis, Nematic electronic structure in the 'parent' state of the iron-based superconductor $Ca(Fe_{1-x}Co_x)_2As_2$, Science **327**, 181 (2010).

[39] M. P. Allan, T.-M. Chuang, F. Massee, Y. Xie, N. Ni, S. L. Bud'ko, G. S. Boebinger, Q. Wang, D. S. Dessau, P. C. Canfield, M. S. Golden, and J. C. Davis, Anisotropic impurity states, quasiparticle scattering and nematic transport in underdoped $Ca(Fe_{1-x}Co_x)_2As_2$, Nat. Phys. **9**, 220 (2013).

[40] E. P. Rosenthal, E. F. Andrade, C. J. Arguello, R. M. Fernandes, L. Y. Xing, X. C. Wang, C. Q. Jin, A. J. Millis, and A. N. Pasupathy, Visualization of electron nematicity and unidirectional antiferroic fluctuations at high temperatures in NaFeAs, Nat. Phys. **10**, 225 (2014).

[41] S. Kasahara, H. J. Shi, K. Hashimoto, S. Tonegawa, Y. Mizukami, T. Shibauchi, K. Sugimoto, T. Fukuda, T. Terashima, A. H. Nevidomskyy, and Y. Matsuda, Electronic nematicity above the structural and superconducting transition in $BaFe_2(As_{1-x}P_x)_2$, Nature (London) **486**, 382 (2012).

[42] L. Stojchevska, T. Mertelj, J.-H. Chu, I. R. Fisher, and D. Mihailovic, Doping dependence of femtosecond quasiparticle relaxation dynamics in $Ba(Fe, Co)_2As_2$ single crystals: Evidence for normal-state nematic fluctuations, Phys. Rev. B **86**, 024519 (2012).

[43] A. Patz, T. Li, S. Ran, R. M. Fernandes, J. Schmalian, S. L. Bud'ko, P. C. Canfield, I. E. Perakis, and J. Wang, Ultrafast observation of critical nematic fluctuations and giant magnetoelastic coupling in iron pnictides, Nat. Commun. **5**, 3229 (2014).

[44] A. Dusza, A. Lucarelli, F. Pfuner, J.-H. Chu, I. R. Fisher, and L. Degiorgi, Anisotropic charge dynamics in detwinned $Ba(Fe_{1-x}Co_x)_2As_2$, Europhys. Lett. **93**, 37002 (2011).

[45] A. Dusza, A. Lucarelli, A. Sanna, S. Massidda, J.-H. Chu, I. R. Fisher, and L. Degiorgi, Anisotropic in-plane optical conductivity in detwinned $Ba(Fe_{1-x}Co_x)_2As_2$, New J. Phys. **14**, 023020 (2012).

[46] M. Nakajima, T. Liang, S. Ishida, Y. Tomioka, K. Kihou, C. H. Lee, A. Iyo, H. Eisaki, T. Kakeshita, T. Ito, and S. Uchida, Unprecedented anisotropic metallic state in undoped iron arsenide $BaFe_2As_2$ revealed by optical spectroscopy, Proc. Natl. Acad. Sci. USA **108**, 12238 (2011).

[47] M. Nakajima, S. Ishida, Y. Tomioka, K. Kihou, C. H. Lee, A. Iyo, T. Ito, T. Kakeshita, H. Eisaki, and S. Uchida, Effect of Co Doping on the In-Plane Anisotropy in the Optical Spectrum of Underdoped $Ba(Fe_{1-x}Co_x)_2As_2$, Phys. Rev. Lett. **109**, 217003 (2012).

[48] W.-L. Zhang, P. Richard, H. Ding, A. S. Sefat, J. Gillett, S. E. Sebastian, M. Khodas, and G. Blumberg, On the origin of the electronic anisotropy in iron pnicitde superconductors, arXiv:1410.6452.

[49] Y. Gallais, R. M. Fernandes, I. Paul, L. Chauviè, Y.-X. Yang, M.-A. Méasson, M. Cazayous, A. Sacuto, D. Colson, and A. Forget, Observation of Incipient Charge Nematicity in $Ba(Fe_{1-x}Co_x)_2As_2$, Phys. Rev. Lett. **111**, 267001 (2013).

[50] J.-H. Chu, H.-H. Kuo, J. G. Analytis, and I. R. Fisher, Divergent nematic susceptibility in an iron arsenide superconductor, Science **337**, 710 (2012).

[51] H.-H. Kuo, M. C. Shapiro, S. C. Riggs, and I. R. Fisher, Measurement of the elastoresistivity coefficients of the underdoped iron-arsenide $Ba(Fe_{0.975}Co_{0.025})_2As_2$, Phys. Rev. B **88**, 085113 (2013).

[52] H.-H. Kuo and I. R. Fisher, Effect of Disorder on the Resistivity Anisotropy Near the Electronic Nematic Phase Transition in Pure and Electron-Doped $BaFe_2As_2$, Phys. Rev. Lett. **112**, 227001 (2014).

[53] The piezotechnique is better performing at $T \geqslant T_s$, because of the reduced dynamic range of the piezo itself at lower temperatures.

[54] C. Mirri, A. Dusza, S. Bastelberger, J.-H. Chu, H.-H. Kuo, I. R. Fisher, and L. Degiorgi, Hysteretic behavior in the optical response of the underdoped Fe-arsenide $Ba(Fe_{1-x}Co_x)_2As_2$ in the electronic nematic phase, Phys. Rev. B **89**, 060501(R) (2014), and Supplemental Material therein.

[55] C. Mirri, A. Dusza, S. Bastelberger, J.-H. Chu, H.-H. Kuo, I. R. Fisher, and L. Degiorgi, Nematic-driven anisotropic electronic properties of underdoped detwinned $Ba(Fe_{1-x}Co_x)_2As_2$ revealed by optical spectroscopy, Phys. Rev. B **90**, 155125 (2014).

[56] Following the detailed discussion in Refs. [50] and [51], strain (ϵ) acts as a field on the nematic order parameter (ψ). Hence, the nematic susceptibility is defined as $\partial\psi/\partial\epsilon$. In a mean-field analysis, this quantity diverges following a Curie-Weiss temperature dependence, with a Weiss temperature below the actual structural transition temperature T_s. In contrast, the quantity $\partial\psi/\partial p$ (determined in Ref. [54]) differs from the actual nematic susceptibility since it involves the elastic compliance of the crystal lattice, and in a mean-field analysis diverges following a Curie-Weiss temperature dependence with a Weiss temperature equal to T_s.

[57] C. Mirri, A. Dusza, S. Bastelberger, M. Chinotti, L. Degiorgi, J.-H. Chu, H.-H. Kuo, and I. R. Fisher, Origin of the Resistive Anisotropy in the Electronic Nematic Phase of $BaFe_2As_2$ Revealed by Optical Spectroscopy, Phys. Rev. Lett. **115**, 107001 (2015).

[58] J.-H. Chu, J. G. Analytis, C. Kucharczyk, and I. R. Fisher, Determination of the phase diagram of the electron-doped superconductor $Ba(Fe_{1-x}Co_x)_2As_2$, Phys. Rev. B **79**, 014506 (2009).

[59] M. Dressel and G. Grüner, *Electrodynamics of Solids* (Cambridge University Press, Cambridge, England, 2002).

[60] W. Z. Hu, J. Dong, G. Li, Z. Li, P. Zheng, G. F. Chen, J. L. Luo, and N. L. Wang, Origin of the Spin Density Wave Instability in AFe_2As_2 (A = Ba, Sr) as Revealed by Optical Spectroscopy, Phys. Rev. Lett. **101**, 257005 (2008).

[61] A. Lucarelli, A. Dusza, F. Pfuner, P. Lerch, J. G. Analytis, J.-H. Chu, I. R. Fisher, and L. Degiorgi, Charge dynamics of Co-doped $BaFe_2As_2$, New J. Phys. **12**, 073036 (2010).

[62] A. Sanna, F. Bernardini, G. Profeta, S. Sharma, J. K. Dewhurst, A. Lucarelli, L. Degiorgi, E. K. U. Gross, and S. Massidda, Theoretical investigation of optical conductivity in $Ba(Fe_{1-x}Co_x)_2As_2$, Phys. Rev. B **83**, 054502 (2011).

[63] Z. P. Yin, K. Haule, and G. Kotliar, Magnetism and charge dynamics in iron pnictides, Nat. Phys. **7**, 294 (2011).

[64] K. Sugimoto, E. Kaneshita, and T. Tohyama, Origin of in-plane anisotropy in optical conductivity for antiferromagnetic metallic phase of iron pnictides, J. Phys. Soc. Jpn. **80**, 033706 (2011).

[65] D. Wu, N. Barišić, P. Kallina, A. Faridian, B. Gorshunov, N. Drichko, L. J. Li, X. Lin, G. H. Cao, Z. A. Xu, N. L. Wang, and M. Dressel, Optical investigations of the normal and

superconducting states reveal two electronic subsystems in iron pnictides, Phys. Rev. B **81**, 100512(R) (2010).

[66] L. Benfatto, E. Cappelluti, L. Ortenzi, and L. Boeri, Extended Drude model and role of interband transitions in the midinfrared spectra of pnictides, Phys. Rev. B **83**, 224514 (2011).

[67] B. Valenzuela, M. J. Calderón, G. León, and E. Bascones, Optical conductivity and Raman scattering of iron superconductors, Phys. Rev. B **87**, 075136 (2013).

[68] M. J. Calderón, L. de' Medici, B. Valenzuela, and E. Bascones, Correlation, doping, and interband effects on the optical conductivity of iron superconductors, Phys. Rev. B **90**, 115128 (2014).

[69] A. A. Schafgans, B. C. Pursley, A. D. LaForge, A. S. Sefat, D. Mandrus, and D. N. Basov, Phonon splitting and anomalous enhancement of infrared-active modes in $BaFe_2As_2$, Phys. Rev. B **84**, 052501 (2011).

[70] It has been previously shown, that pressures of about 10 MPa, as uniaxial pressure effectively felt by the sample, are enough in order to lead to a single domain specimen (e.g., see Fig. 4 of Ref. [1]).

[71] M. A. Tanatar, E. C. Blomberg, A. Kreyssig, M. G. Kim, N. Ni, A. Thaler, S. L. Bud'ko, P. C. Canfield, A. I. Goldman, I. I. Mazin, and R. Prozorov, Uniaxial-strain mechanical detwinning of $CaFe_2As_2$ and $BaFe_2As_2$ crystals: Optical and transport study, Phys. Rev. B **81**, 184508 (2010).

[72] Unless stated otherwise, the displayed anisotropy corresponds to the ratio, between the *a* and *b* axes, of the measured/calculated physical quantity.

[73] W. L. Yang, A. P. Sorini, C.-C. Chen, B. Moritz, W.-S. Lee, F. Vernay, P. Olalde-Velasco, J. D. Denlinger, B. Delley, J.-H. Chu, J. G. Analytis, I. R. Fisher, Z. A. Ren, J. Yang, W. Lu, Z. X. Zhao, J. van den Brink, Z. Hussain, Z.-X. Shen, and T. P. Devereaux, Evidence for weak electronic correlations in iron pnictides, Phys. Rev. B **80**, 014508 (2009).

[74] V. I. Anisimov, E. Z. Kurmaev, A. Moewes, and I. A. Izyumov, Strength of correlations in pnictides and its assessment by theoretical calculations and spectroscopy experiments, Physica C **469**, 442 (2009).

[75] S. Zhou and Z. Wang, Electron Correlation and Spin Density Wave Order in Iron Pnictides, Phys. Rev. Lett. **105**, 096401 (2010).

[76] A. Kutepov, K. Haule, S. Y. Savrasov, and G. Kotliar, Self-consistent GW determination of the interaction strength: Application to the iron arsenide superconductors, Phys. Rev. B **82**, 045105 (2010).

[77] A. A. Schafgans, S. J. Moon, B. C. Pursley, A. D. LaForge, M. M. Qazilbash, A. S. Sefat, D. Mandrus, K. Haule, G. Kotliar, and D. N. Basov, Electronic Correlations and Unconventional Spectral Weight Transfer in the High-Temperature Pnictide $BaFe_{2-x}Co_xAs_2$ Superconductor using Infrared Spectroscopy, Phys. Rev. Lett. **108**, 147002 (2012).

[78] Q. Si, Iron pnictide superconductors: Electrons on the verge, Nat. Phys. **5**, 629 (2009).

[79] S. Liang, G. Alvarez, C. Şen, A. Moreo, and E. Dagotto, Anisotropy of Electrical Transport in Pnictide Superconductors Studied using Monte Carlo Simulations of the Spin-Fermion Model, Phys. Rev. Lett. **109**, 047001 (2012).

[80] B. Valenzuela, E. Bascones, and M. J. Calderón, Conductivity Anisotropy in the Antiferromagnetic State of Iron Pnictides, Phys. Rev. Lett. **105**, 207202 (2010).

[81] P. Prelovšek, I. Sega, and T. Tohyama, Analysis of the transport properties of iron pnictides: Spin-fluctuation scenario, Phys. Rev. B **80**, 014517 (2009).

[82] R. M. Fernandes, E. Abrahams, and J. Schmalian, Anisotropic In-Plane Resistivity in the Nematic Phase of the Iron Pnictides, Phys. Rev. Lett. **107**, 217002 (2011).

[83] M. Breitkreiz, P. M. R. Brydon, and C. Timm, Resistive anisotropy due to spin-fluctuation scattering in the nematic phase of iron pnictides, Phys. Rev. B **90**, 121104(R) (2014).

[84] M. N. Gastiasoro, P. J. Hirschfeld, and B. M. Andersen, Origin of electronic dimers in the spin-density wave phase of Fe-based superconductors, Phys. Rev. B **89**, 100502(R) (2014).

[85] M. N. Gastiasoro, I. Paul, Y. Wang, P. J. Hirschfeld, and B. M. Andersen, Emergent Defect States as a Source of Resistivity Anisotropy in the Nematic Phase of Iron Pnictides, Phys. Rev. Lett. **113**, 127001 (2014).

[86] Y. Wang, M. N. Gastiasoro, B. M. Andersen, M. Tomić, H. O. Jeschke, R. Valentí, I. Paul, and P. J. Hirschfeld, Effects of Lifshitz Transition on Charge Transport in Magnetic Phases of Fe-Based Superconductors, Phys. Rev. Lett. **114**, 097003 (2015).

[87] S. Liang, C. B. Bishop, A. Moreo, and E. Dagotto, Isotropic in-plane quenched disorder and dilution induce a robust nematic state in electron-doped pnictides, Phys. Rev. B **92**, 104512 (2015).

[88] M. Schütt, J. Schmalian, and R. M. Fernandes, Origin of the DC and AC conductivity anisotropy in iron-based superconductors: scattering rate versus spectral weight effects, arXiv:1512.02259, (2015).